JM PAPERS

Experimental investigations of linear and nonlinear periodic travelling waves in a viscous fluid conduit

Yifeng Mao[1,†] and Mark A. Hoefer[1]

[1]Department of Applied Mathematics, University of Colorado, Boulder, CO 80309, USA

Conduits generated by the buoyant dynamics between two miscible Stokes fluids with high viscosity contrast, a type of core–annular flow, exhibit a rich nonlinear wave dynamics. However, little is known about the fundamental wave dispersion properties of the medium. In the present work, a pump is used to inject a time-periodic flow that results in the excitation of propagating small- and large-amplitude periodic travelling waves along the conduit interface. This wavemaker problem is used as a means to measure the linear and nonlinear dispersion relations and corresponding periodic travelling wave profiles. Measurements are favourably compared with predictions from a fully nonlinear, long-wave model (the conduit equation) and the analytically computed linear dispersion relation for two-Stokes flow. A critical frequency is observed, marking the threshold between propagating and non-propagating (spatially decaying) waves. Measurements of wave profiles and the wavenumber–frequency dispersion relation quantitatively agree with wave solutions of the conduit equation. An upshift from the conduit equation's predicted critical frequency is observed and is explained by incorporating a weak recirculating flow into the full two-Stokes flow model. When the boundary condition corresponds to the temporal profile of a nonlinear periodic travelling wave solution of the conduit equation, weakly nonlinear and strongly nonlinear, cnoidal-type waves are observed that quantitatively agree with the conduit nonlinear dispersion relation and wave profiles. This wavemaker problem is an important precursor to the experimental investigation of more general boundary value problems in viscous fluid conduit nonlinear wave dynamics.

Key words: Stokesian dynamics, pattern formation

† Email address for correspondence: yifeng.mao@colorado.edu

1. Introduction

The wavemaker problem consists of waves launched from a boundary into a medium at rest. It is a fundamental problem for inviscid flows with physical applications, including surface waves in reservoirs or lakes produced by the movement of a solid body (Chwang 1983*b*). In the laboratory, wavemakers provide the means to generate finite-amplitude water waves (Chwang 1983*a*). Some examples highlighting the rich variety of nonlinear wave dynamics that is possible include the generation of cnoidal waves (Goring & Raichlen 1980), interacting undular bores (Trillo *et al.* 2016) and evidence of a soliton gas (Redor *et al.* 2019) from the fission of a sinusoidal wave and the controlled generation of an isolated rogue wave (Chabchoub, Hoffmann & Akhmediev 2011; Tikan *et al.* 2022).

This paper presents an alternative fluid medium, called a conduit, in which to investigate the wavemaker problem in the linear and nonlinear regimes. The pressure-driven, buoyant, core–annular flow between two miscible Stokes fluids with a small core-to-annular fluid viscosity ratio is a simple, conducive laboratory setting for the quantitative experimental study of nonlinear wave propagation (Olson & Christensen 1986; Scott, Stevenson & Whitehead 1986; Helfrich & Whitehead 1990; Maiden *et al.* 2016, 2020). This setting is quite different from more traditional core–annular flows, such as oil–water, subject to non-negligible inertial and surface tension effects resulting in a variety of instabilities (Joseph *et al.* 1997). Instead, we operate in a vanishing Reynolds number regime where the flow is convectively unstable (d'Olce *et al.* 2009) and can be effectively interpreted as a deformable, fluid-filled pipe (Olson & Christensen 1986; Lowman & Hoefer 2013) due to very slow mass diffusion across the conduit interface (Maiden *et al.* 2016). Conduits model viscously deformable media in a variety of physical environments such as magma in the Earth's mantle (Whitehead & Helfrich 1990) and channelized water flow under glaciers (Stubblefield, Spiegelman & Creyts 2020). A schematic of the flow configuration is shown in figure 1.

In traditional pressure-driven core–annular flows, finite-amplitude dynamics can be studied in the long-wavelength regime using an approximate interfacial wave model consisting of nonlinear advective and dissipative terms such as those asymptotically derived in Camassa & Ogrosky (2015). These models can be viewed as generalizations of the famous Kuramoto–Sivashinsky equation (Sivashinsky 1977; Kuramoto 1978), which exhibits spatio-temporal chaos. In contrast, the viscous core–annular flow of a pressure-driven Stokes core fluid within an annulus of another, miscible, heavier Stokes fluid is accurately modelled by the so-called conduit equation

$$A_t + (A^2)_z - (A^2(A^{-1}A_t)_z)_z = 0, \tag{1.1}$$

for the normalized, axisymmetric cross-sectional area A of a fluid conduit at non-dimensional vertical height z and time t. The conduit equation is an expression of mass conservation subject to buoyancy-induced nonlinear advection and nonlinear, non-local dispersion due to interfacial stresses that is obtained from the two-fluid Navier–Stokes equations in the small Reynolds number, small core-to-annular viscosity ratio and long-wavelength regime with no assumption on wave amplitude (Olson & Christensen 1986; Lowman & Hoefer 2013). Unlike models of traditional core–annular flows, this third-order dispersive nonlinear wave equation is more closely analogous to the Korteweg-de Vries equation of shallow water wave fame (Korteweg & de Vries 1895).

Much as in the aforementioned hydrodynamic wavemaker case, the viscous conduit is a laboratory environment for the study of a variety of nonlinear wave dynamics. Past experimental studies include solitary waves (Olson & Christensen 1986; Scott *et al.* 1986) and their interactions (Helfrich & Whitehead 1990; Lowman, Hoefer & El 2014),
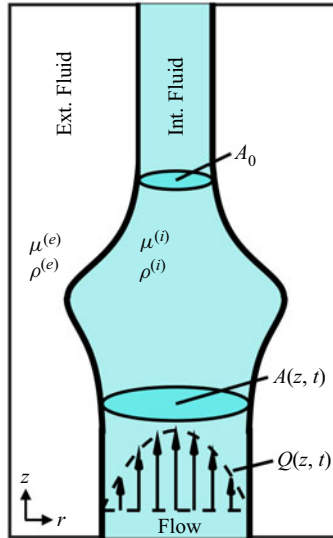
Figure 1. Schematic of the core–annular flow configuration. The interior fluid rises buoyantly within the exterior fluid with densities $\rho^{(i)} < \rho^{(e)}$ and viscosities $\mu^{(i)} \ll \mu^{(e)}$, respectively. The vertical volumetric flow rate is $Q(z, t)$, the cross-sectional area of the interface is $A(z, t)$ and A_0 is the background, mean area of the conduit.

periodic waves (Olson & Christensen 1986; Kumagai & Kurita 1998), solitary wave fission (Anderson, Maiden & Hoefer 2019; Maiden *et al.* 2020), dispersive shock waves (DSWs) (Maiden *et al.* 2016) and interactions between solitary waves and DSWs (Maiden *et al.* 2018). Quantitative observational agreement with the conduit equation (1.1) has been achieved in certain regimes. But such agreement has largely been confined to the long-wave, nonlinear regime. Herein, we experimentally investigate the generation of long and short periodic travelling waves in a viscous fluid conduit using a wavemaker with a view toward understanding their fundamental properties.

Periodic wavetrains have already been observed and studied in viscous fluid conduits. Some of the earliest studies generated periodic waves by either quickly increasing the injection rate from one constant value to another constant value (Scott *et al.* 1986; Kumagai & Kurita 1998) or tracking the periodic waves that trail a rising diapir from a plume of injected fluid (Olson & Christensen 1986). However, since the injection rate was held constant after the initial change, both scenarios involve a different dynamics than we consider here. In the first case, we now understand that a step up in injection rate from a non-zero previous rate results in a DSW consisting of a slowly varying, expanding periodic travelling wave that ultimately returns to a constant injection rate, i.e. it is transient (Maiden *et al.* 2016). In the latter case, it is likely that an oscillatory (absolute) instability (d'Olce *et al.* 2009) developed due to sufficiently large injection rate rather than the convective instability regime in which we operate. In this work, we controllably create high-quality linear and nonlinear periodic travelling waves by use of a carefully selected time-periodic injection rate by evaluating exact periodic travelling wave solutions of the model conduit equation.

The major objective of this work is the reliable generation of both linear and nonlinear, cnoidal-type waves from a wavemaker. Laboratory measurement constrained by boundary control is realized by injecting an interior fluid of lower viscosity and lower density into a more viscous exterior fluid using a piston pump. Limitations are investigated, and the

experiment is compared with the theory of the boundary value problem for the conduit equation. We find that, although the exact periodic travelling wave solutions to the conduit equation exhibit quantitative agreement with our experimental observations, a deviation in the linear dispersion relation occurs for sufficiently short waves. In order to describe the linear waves in the shorter-wavelength regime, we obtain the exact solution for two-Stokes flow linear interfacial wave propagation. Previous work by Yih (1963, 1967) and Hickox (1971) studied the linear instability of core–annular flows for the Navier–Stokes equations. Within a parameter regime consistent with our experimental conditions, the instability has been shown to be convective (d'Olce *et al.* 2009; Selvam *et al.* 2009). However, none of these works obtained an analytical solution to the problem, instead relying upon numerical solutions. Herein, we develop a model for recirculating viscous core–annular flows in our experiments and obtain the exact solution to the Stokes equations for azimuthally symmetric, small-amplitude perturbations. The two-Stokes linear dispersion relation is shown to agree with the conduit equation's linear dispersion relation in the limit of high viscosity contrast and long waves.

The paper is structured as follows. First, we provide some background material on the conduit equation and periodic travelling waves. Then we derive the exact linear dispersion relation for two-Stokes core–annular flow in § 2. Analytical results for an idealized recirculating flow with azimuthally symmetric linear interfacial waves and their asymptotic expansions are presented. Section 3 describes linear modulation theory applied to the initial-boundary value problem for both the conduit equation and two-Stokes flow. In § 4, experimental methods and analysis of linear and nonlinear periodic travelling waves in a viscous fluid conduit are provided. Finally, we conclude in § 5.

1.1. *The conduit equation*

The conduit equation (1.1) is an accurate partial differential equation model of conduit interfacial waves whose mathematical structure and solutions have been analysed (Harris & Clarkson 2006; Simpson & Weinstein 2008; Maiden & Hoefer 2016; Johnson & Perkins 2020).

The conduit equation exhibits solutions that are reminiscent of the Korteweg–de Vries (KdV) and Benjamin–Bona–Mahoney (BBM) equations, both models of shallow water waves. In fact, the conduit equation can be reduced to the BBM and KdV equations for long waves and weak nonlinearity. Let

$$T = \delta^{1/2}t, \quad Z = \delta^{1/2}z, \tag{1.2a,b}$$

and

$$A(z, t) = 1 + \delta u(Z, T) + \dots, \tag{1.3}$$

where $\delta \ll 1$ is the small amplitude parameter and $u(Z, T)$ is the scaled, leading-order deviation in cross-sectional area. Insertion of this ansatz into (1.1) and keeping the leading and first-order terms results in the BBM equation (Benjamin, Bona & Mahony 1972)

$$u_T + 2u_Z + 2\delta uu_Z - \delta u_{ZZT} = 0. \tag{1.4}$$

Since $u_T = -2u_Z + O(\delta)$ implies $u_{ZZT} = -2u_{ZZZ} + O(\delta)$, we obtain the KdV equation $u_T + 2u_Z + 2\delta uu_Z + 2\delta u_{ZZZ} = 0$ to the same order of accuracy (Whitehead & Helfrich 1986). Hence, both the BBM and KdV equations are asymptotically equivalent to the conduit equation (1.1) in the weakly nonlinear, long-wavelength regime. Notably, the BBM equation (1.4) with $\delta = 1$ has the same linear dispersion relation as the conduit equation (1.1) on a unit-mean background.

The travelling wave solutions of both the BBM and KdV equations may be expressed in terms of the Jacobi cosine elliptic function cn, the so-called cnoidal wave solutions (Korteweg & de Vries 1895), as

$$
\left.
\begin{aligned}
u(Z, T) &= \beta + (\gamma - \beta)\mathrm{cn}^2\left[\left(\frac{\gamma - \alpha}{6\chi}\right)^{1/2}(Z - cT); m\right], \\
c &= \frac{2\delta(\alpha + \beta + \gamma)}{3} + 2, \quad m = \frac{\gamma - \beta}{\gamma - \alpha},
\end{aligned}
\right\}
\tag{1.5}
$$

where α, β, γ are independent, free parameters. The only difference between the KdV and BBM cnoidal solutions is in the wavenumber coefficient χ: $\chi_{KdV} = 2$, $\chi_{BBM} = c$. In the limit $\beta \to \alpha$ with $\beta \neq \gamma$, (1.5) reduces to a sech^2 solitary wave solution and in the small-amplitude limit $0 < \gamma - \beta \ll 1$, (1.5) becomes a sinusoidal travelling wave.

1.2. *The wavemaker problem and periodic travelling wave solutions*

For a time-harmonic boundary condition in the linear regime, the Sommerfeld radiation condition (Sommerfeld 1912, 1949) can be used to select a particular solution, either a propagating wave or a spatially decaying wave, by requiring a causal solution with only outgoing waves at infinity. The cross-over between the two behaviours occurs at zero group velocity. This condition has been applied to many problems in fluid dynamics and elsewhere (see, e.g. Bühler 2014) and will be applied to the conduit equation.

The conduit equation (1.1) obeys the scaling invariance

$$
A^* = \frac{A}{\bar{A}}, \quad z^* = \bar{A}^{-1/2}z, \quad t^* = \bar{A}^{1/2}t,
\tag{1.6a-c}
$$

where $\bar{A} > 0$, which leaves (1.1) invariant. Owing to this scaling invariance, we will, without loss of generality, assume that the periodic travelling wave has unit mean. In this work, we study the wavemaker problem for a viscous fluid conduit subject to a specially chosen time-dependent, periodic input with amplitude a and injection frequency ω_0 at the boundary. The wavemaker initial-boundary value problem is

$$
\left.
\begin{aligned}
A(z, 0) &= 1, \quad z \geqslant 0, \\
A(0, t) &= 1 + f(t), \quad t \geqslant 0, \quad f(t + T_0) = f(t), \quad t > 0, \quad T_0 = \frac{2\pi}{\omega_0},
\end{aligned}
\right\}
\tag{1.7}
$$

where $f(t)$ is the zero mean periodic profile with frequency $\omega_0 > 0$, $f(0) = f'(0) = 0$, $\int_0^{T_0} f(t)\,dt = 0$.

Conduit periodic travelling wave solutions satisfy $A(z, t) = \phi(\theta)$, $\theta = kz - \omega t$, $\phi(\theta + 2\pi) = \phi(\theta)$ for $\theta \in \mathbb{R}$, wavenumber $k \geq 0$, and frequency $\omega \geq 0$ subject to the nonlinear ordinary differential equation (Olson & Christensen 1986)

$$
-\omega\phi' + k(\phi^2)' + \omega k^2(\phi^2(\phi^{-1}\phi')')' = 0.
\tag{1.8}
$$

Integrating (1.8) twice results in

$$
(\phi')^2 = g(\phi) \equiv -\frac{2}{k^2}\phi - \frac{2}{\omega k}\phi^2 \ln \phi + c_1 + c_2\phi^2,
\tag{1.9}
$$

where $c_{1,2}$ are integration constants. Conduit solitary wave solutions are asymptotically stable (Simpson & Weinstein 2008) and periodic travelling waves are modulationally stable for sufficiently long wavelengths (Maiden & Hoefer 2016; Johnson & Perkins 2020).

Upon linearization of (1.1) as $A(z, t) - 1 \propto \cos(kz - \omega t)$, the conduit equation exhibits a bounded dispersion relation

$$\omega = \frac{2k}{1 + k^2}. \tag{1.10}$$

For the wavemaker problem, it is helpful to invert the linear dispersion relation (1.10) and solve for $k(\omega)$. In order to select the correct branch, we apply the radiation condition (positive group velocity or spatial decay) to obtain

$$k(\omega) = \begin{cases} \dfrac{1 - \sqrt{1 - \omega^2}}{\omega}, & 0 < \omega \leqslant 1 \\ \dfrac{1 + i\sqrt{\omega^2 - 1}}{\omega}, & \omega > 1 \end{cases}, \tag{1.11}$$

where wavenumbers k for frequencies $0 < \omega \leqslant 1$ are real, implying steady wave propagation. For $\omega > 1$, $k(\omega)$ exhibits a positive imaginary part so that these waves spatially decay (equivalent to Gaster 1962). The frequency $\omega_{cr} = 1$ is therefore the critical frequency, above which waves decay and get arrested. The corresponding critical wavenumber $k_{cr} = 1$ satisfies $k_{cr} = k(\omega_{cr})$.

In the weakly nonlinear regime, we can obtain approximate periodic travelling wave solutions when the amplitude is small and the wavenumber is sufficiently far away from 0. The weakly nonlinear approximation with three harmonics takes the form

$$\phi(\theta; k, a) = 1 + \frac{a}{2}\cos(\theta) + \frac{1 + k^2}{48k^2}a^2\cos(2\theta) + \frac{1 + k^2}{1536k^4}a^3\cos(3\theta) + O(a^4), \tag{1.12}$$

where $\theta = kz - \omega t$, the amplitude $0 < a \ll 1$, the wavenumber $k^2 \gg a$ and the frequency ω is approximately

$$\omega(k, a) = \frac{2k}{1 + k^2} + a^2 \frac{1 - 8k^2}{48k(1 + k^2)} + O(a^4). \tag{1.13}$$

Alternatively, we can express the weakly nonlinear expansions in terms of ω and obtain

$$\phi(\theta, \omega, a) = 1 + \frac{a}{2}\cos(\theta) + \frac{a^2}{24\left(1 - \sqrt{1 - \omega^2}\right)}\cos(2\theta)$$
$$+ \frac{\left(-1 - \sqrt{1 - \omega^2}\right)a^3}{768\left(-2 + \omega^2 + 2\sqrt{1 - \omega^2}\right)}\cos(3\theta) + \ldots, \tag{1.14a}$$

$$k(\omega, a) = \frac{1 - \sqrt{1 - \omega^2}}{\omega} + \frac{\left(-9 + \dfrac{7}{\sqrt{1 - \omega^2}}\right)}{96\omega}a^2 + \ldots, \tag{1.14b}$$

for $0 < \omega < 1$. The induced mean occurs at $O(a^2)$ and must be taken into account when nonlinear modulations are considered (Maiden & Hoefer 2016).
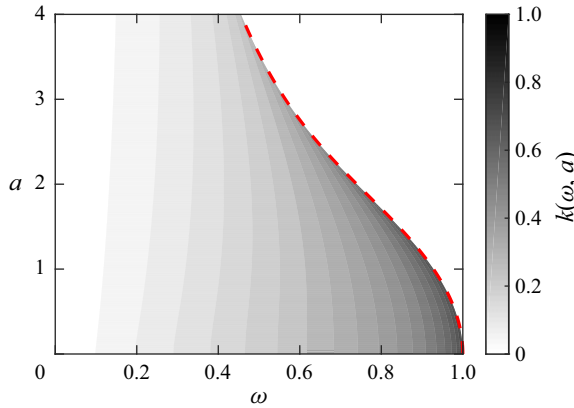
954 A14-6

Figure 2. Contour plot of numerically computed conduit dispersion relation $k(\omega, a)$. Beyond the red dashed line, no real $k(\omega, a)$ is obtained.

The nonlinear dispersion relation is explicitly expressed in terms of three roots $0 < u_1 < u_2 < u_3$ of $g(\phi)$ in (1.9) (Lowman & Hoefer 2013) and phase velocity U so that

$$\exp U = u_1^{u_1^2(u_2+u_3)/(u_3-u_1)(u_2-u_1)} u_2^{-u_2^2(u_3+u_1)/(u_3-u_2)(u_2-u_1)} u_3^{u_3^2(u_2+u_1)/(u_3-u_1)(u_3-u_2)}. \tag{1.15}$$

The numerically computed conduit nonlinear dispersion relation $\omega = kU$ is presented in figure 2, where the red dashed line corresponds to the edge of the existence region. The wave amplitude, wavenumber and mean are given by

$$a = u_3 - u_2, \quad k = \pi \left(\int_{u_2}^{u_3} \frac{\mathrm{d}u}{\sqrt{g(u)}} \right)^{-1}, \quad \bar{\phi} = \frac{k}{\pi} \int_{u_2}^{u_3} \frac{u\,\mathrm{d}u}{\sqrt{g(u)}}, \tag{1.16a–c}$$

where $g(u)$ is defined in equation (1.9). The limits $u_2 \to u_1$ and $u_2 \to u_3$ correspond to the solitary wave and linear, harmonic limits, respectively. These periodic travelling wave solutions are analogous to the cnoidal solutions of KdV and BBM (1.5) and therefore we will refer to them as cnoidal-like throughout this work.

2. Two-Stokes flow

Since the conduit equation (1.1) and its linear dispersion relation (1.10), (1.11) are derived under long wavelength assumptions, we now seek a more accurate description of linear waves by analysing the free interface between two-Stokes fluids.

2.1. *Primary recirculating flow*

Interfacial waves generated by the buoyant dynamics between two miscible Stokes fluids with a small viscosity ratio $\epsilon = \mu^{(i)}/\mu^{(e)}$ are described by continuity equations for mass conservation and Stokes equations for momentum conservation

$$\nabla \cdot \tilde{\boldsymbol{u}}^{(i,e)} = 0, \tag{2.1a}$$

$$-\nabla \tilde{p}^{(i,e)} + \nabla \cdot \tilde{\boldsymbol{\sigma}}^{(i,e)} = 0, \tag{2.1b}$$

for the interior and exterior fluids, denoted by superscripts i or e, respectively. The velocity fields $\tilde{\boldsymbol{u}}^{(i,e)} = (\tilde{u}_{\tilde{r}}^{(i,e)}, \tilde{u}_{\tilde{z}}^{(i,e)})$ are given in cylindrical coordinates assuming

954 A14-7

azimuthal symmetry. The pressure deviation from hydrostatic is $\tilde{p}^{(i,e)}$ and the deviatoric stress tensor is $\tilde{\boldsymbol{\sigma}}^{(i,e)} = \mu^{(i,e)}[\nabla\tilde{\boldsymbol{u}} + (\nabla\tilde{\boldsymbol{u}})^{\mathrm{T}}]$, where $\mu^{(i,e)}$ denotes the fluid viscosity. The kinematic boundary condition between the two fluids at $\tilde{r} = \tilde{R}(z,t)$ incorporates the time dynamics

$$\tilde{u}_{\tilde{r}}^{(i)} = \frac{\partial \tilde{R}}{\partial \tilde{t}} + \tilde{u}_{\tilde{z}}^{(i)}\frac{\partial \tilde{R}}{\partial \tilde{z}}, \quad \tilde{r} = \tilde{R}(\tilde{z}, \tilde{t}). \tag{2.2a,b}$$

The remaining boundary conditions include the continuity of normal and tangential velocities

$$[\tilde{\boldsymbol{u}} \cdot \hat{\tilde{\boldsymbol{n}}}_c]_j = [\tilde{\boldsymbol{u}} \cdot \hat{\tilde{\boldsymbol{t}}}_c]_j = 0, \quad \tilde{r} = \tilde{R}(\tilde{z}, \tilde{t}), \tag{2.3a,b}$$

and continuity of normal and tangential stresses

$$[\hat{\tilde{\boldsymbol{n}}}_c \cdot \tilde{\boldsymbol{T}} \cdot \hat{\tilde{\boldsymbol{n}}}_c]_j = [\hat{\tilde{\boldsymbol{t}}}_c \cdot \tilde{\boldsymbol{T}} \cdot \hat{\tilde{\boldsymbol{n}}}_c]_j = 0, \quad \tilde{r} = \tilde{R}(\tilde{z}, \tilde{t}), \tag{2.4a,b}$$

where $[\,]_j$ represents the difference in the exterior and interior fluid quantities, $\hat{\tilde{\boldsymbol{n}}}_c$ is the outward pointing unit normal to the interface and $\hat{\tilde{\boldsymbol{t}}}_c$ is the unit tangent to the interface. Here, $\tilde{\boldsymbol{T}}^{(i,e)} = \tilde{\boldsymbol{\sigma}}^{(i,e)} - \boldsymbol{I}\tilde{p}^{(i,e)}$ is the stress tensor and $\boldsymbol{I}$ denotes the identity operator. No-slip and no-penetration boundary conditions at the outer wall $\tilde{r} = \tilde{D}$ require $\tilde{u}_{\tilde{z}}^{(e)}(\tilde{D}) = 0$ and $\tilde{u}_{\tilde{r}}^{(e)}(\tilde{D}) = 0$. Boundary conditions along the symmetry axis are imposed as

$$\frac{\partial \tilde{u}_{\tilde{z}}^{(i)}}{\partial \tilde{r}} = 0, \quad \tilde{u}_{\tilde{r}}^{(i)} = 0, \quad \frac{\partial \tilde{p}^{(i)}}{\partial \tilde{r}} = 0, \quad \text{at } \tilde{r} = 0. \tag{2.5}$$

A non-dimensionalization that leads to a maximal balance between buoyancy and viscous stress effects taking vertical length scale L, velocity scale U and time scale T as $\epsilon \to 0$ is (Lowman & Hoefer 2013)

$$r = \epsilon^{-1/2}\tilde{r}/L, \quad z = \tilde{z}/L, \quad t = \tilde{t}/T, \tag{2.6a}$$

$$\boldsymbol{u}^{(i,e)} = \tilde{\boldsymbol{u}}^{(i,e)}/U, \tag{2.6b}$$

$$p^{(i,e)} = \frac{\tilde{p}^{(i,e)} - \tilde{p}_0}{\Pi}, \quad \Pi = \mu^{(i)}U/L, \tag{2.6c}$$

$$\boldsymbol{\sigma}^{(i,e)} = (L/\mu^{(i,e)}U)\tilde{\boldsymbol{\sigma}}^{(i,e)}, \tag{2.6d}$$

where $\tilde{p}_0$ is a constant reference pressure. The vertical spatial variation L is assumed to be longer than the radial length scale R_0. With constant conduit radius R_0, the scales are defined as

$$L = R_0/\sqrt{8\epsilon}, \quad U = \frac{gR_0^2\Delta}{8\mu^{(i)}}, \quad T = L/U, \quad \Omega = \frac{2\pi}{T}, \tag{2.7a–d}$$

where $\Delta = \rho^{(e)} - \rho^{(i)}$ is the difference in the fluid densities. Substituting the above scalings into the dimensional equations represented by the tilde notation, the non-dimensional continuity and linear momentum equations for the interior and exterior fluid are obtained (see Appendix A).

Steady flow requires only that the axial velocity and pressure have initial values different from zero and the vertical velocity is independent of z, i.e. $u_{r,0}^{(i)} = u_{r,0}^{(e)} = 0$,

954 A14-8

$\partial u_{z,0}^{(i)}/\partial z = \partial u_{z,0}^{(e)}/\partial z = 0$. Collecting the governing equations as well as the boundary conditions, we obtain the solution for the primary flow

$$p_0^{(i)} = (\lambda - 1)z + \Lambda(t), \tag{2.8a}$$

$$u_{z,0}^{(i)} = \frac{(\lambda - 1)}{4}(r^2 - \eta^2) + \frac{\epsilon\lambda}{4}(\eta^2 - D^2) + \frac{\epsilon\eta^2}{2}\ln\frac{D}{\eta}, \tag{2.8b}$$

$$p_0^{(e)} = \lambda z + \Lambda(t), \tag{2.8c}$$

$$u_{z,0}^{(e)} = \epsilon\left(\frac{\lambda}{4}(r^2 - D^2) + \frac{\eta^2}{2}\ln\frac{D}{r}\right), \tag{2.8d}$$

with external fluid pressure gradient λ, internal fluid pressure gradient $\lambda - 1$ and interfacial radius η. Pressure is determined up to an arbitrary function of time $\Lambda(t)$. Since the interior and exterior pressures only play roles in the normal stress balance condition (2.4a,b) (see also (A5a)) and $\Lambda(t)$ cancels in the equation, we set $\Lambda(t) = 0$ without loss of generality. The vertical volumetric flow rates of the interior and exterior flows through a cross-section normal to the z axis are

$$Q^{(i)} = 2\pi\int_0^\eta u_{z,0}^{(i)}(r)r\,\mathrm{d}r$$
$$= \frac{\pi}{8}\left(1 - \lambda + 2\epsilon\lambda - 2\epsilon\lambda\frac{D^2}{\eta^2} + 4\epsilon\ln\frac{D}{\eta}\right)\eta^4, \tag{2.9a}$$

$$Q^{(e)} = 2\pi\int_\eta^D u_{z,0}^{(e)}(r)r\,\mathrm{d}r$$
$$= -\frac{\pi}{8}\epsilon\left(2 + \lambda - 2(1 + \lambda)\frac{D^2}{\eta^2} + \lambda\frac{D^4}{\eta^4} + 4\ln\frac{D}{\eta}\right)\eta^4. \tag{2.9b}$$

In the case of a motionless external fluid so that $\epsilon = 0$ and $\lambda = 0$, the interior flow rate is $Q^{(i)} = (\pi/8)\eta^4$, which, upon dimensionalization (2.7a–d) results in the Poiseuille, pipe flow scaling law $R_0^4 = (8\mu^{(i)}/\pi g\Delta)Q_0$, where Q_0 is the interior fluid injection rate. Note that the external pressure gradient λ is a parameter that is constrained by the direction of fluid flow. Previous studies that derived the conduit equation assumed a high viscosity contrast ($\epsilon \ll 1$), a zero external pressure gradient ($\lambda = 0$) and an infinitely far outer wall ($D \to \infty$). However, in this work, ϵ and λ, as well as D are adapted to model our experiments by introducing an idealized recirculating flow in which the interior fluid rises upward, dragging some of the exterior fluid with it, while the rest of the exterior fluid flows downward. Evaluating the sign of $u_{z,0}^{(e)}(r)$ for r near η and D dictates that

$$\left(\frac{\eta}{D}\right)^2 < \lambda < \frac{2\eta^2\ln(D/\eta)}{D^2 - \eta^2}, \tag{2.10}$$

for recirculating flow. So far, we have only specified the vertical flow directions for the interior and exterior fluids of an infinitely long conduit. In order to model flow recirculation, we need to appeal to the observed fluid dynamics in our experimental apparatus. The rising interior fluid is observed to pool at the very top of the fluid column, creating a less dense, lower viscosity fluid layer above the exterior fluid (see figure 6(a) for a schematic). On the other hand, the exterior fluid entrained by the rising

interior fluid is observed to recirculate downward and, upon reaching the bottom of the column, recirculates upward (see the supplementary material movies available at https://doi.org/10.1017/jfm.2022.993). We model this dynamics by invoking the additional requirement of mass conservation for the exterior fluid (i.e. $Q^{(e)} = 0$ in (2.9b)), resulting in the external pressure gradient

$$\lambda = \frac{2\eta^2(D^2 - \eta^2 - 2\eta^2 \ln(D/\eta))}{(D^2 - \eta^2)^2}. \tag{2.11}$$

The validity of the requirement (2.11) will be discussed in § 4.4 using experimental measurements.

2.2. *Linear dispersion relation*

The linear dispersion relation for waves on a straight conduit in two-Stokes flow is investigated by linearizing about the primary flow. Following the procedure as introduced in Batchelor & Gill (1962) and Hickox (1971), first-order velocities and pressures are written as

$$\boldsymbol{u}_1^{(i)} = [g_z(r), i\epsilon^{1/2}g_r(r)] \exp(i(kz - \omega t)), \tag{2.12a}$$

$$\boldsymbol{u}_1^{(e)} = [\epsilon G_z(r), i\epsilon^{1/2}G_r(r)] \exp(i(kz - \omega t)), \tag{2.12b}$$

$$p_1^{(i)} = h(r) \exp(i(kz - \omega t)), \tag{2.12c}$$

$$p_1^{(e)} = H(r) \exp(i(kz - \omega t)). \tag{2.12d}$$

The ϵ scalings of the exterior and interior velocity perturbations are chosen to reflect tangential stress balance and the kinematic boundary condition. We assume a constant conduit radius η subject to a small disturbance so that

$$R(z, t) = \eta + a \exp(i(kz - \omega t)), \quad |a| \ll 1. \tag{2.13}$$

Solving the governing equations directly and applying the boundary conditions, the eigenfunctions g_r, g_z, h and G_r, G_z, H are obtained in terms of a linear algebraic system given in Appendix B. Analytically, inverting the 6 by 6 matrix leads to overly burdensome expressions, so we either evaluate the linear system numerically or consider its asymptotics for small ϵ. The linear dispersion relation is given by the kinematic boundary condition as

$$\omega(k) = ku_{z,0}^{(i)}(\eta) - g_r(\eta, k). \tag{2.14}$$

In regions where (2.14) is monotonic in k, we can obtain $k(\omega)$ for consideration of the wavemaker problem. In the vicinity of $\omega_k = 0$, we use the radiation condition to select the appropriate branch. Selecting $\eta = \sqrt{8}$ for convenience when comparing with the $\epsilon \to 0$ dispersion relation (1.11), example dispersion curves for waves on a unit-mean background are shown in figure 3. The maximum of $\text{Re}(k(\omega))$ occurs at the critical frequency $\omega = \omega_{cr}$, defined by the group velocity $c_g(\omega_{cr}) = d\omega/dk(\omega_{cr}) = 0$, above which $k(\omega)$ incorporates a non-zero imaginary part and the wave is spatially damped. The corresponding critical wavenumber is $k_{cr} = k(\omega_{cr})$. In the experiments reported in § 4.4, $\epsilon > 0.01$ and the critical frequency is subject to a deviation from 1.

Consider the limit $\epsilon \to 0$. In order for the leading-order behaviour of the two-Stokes system to be well approximated by the conduit dynamics, we require a maximal balance
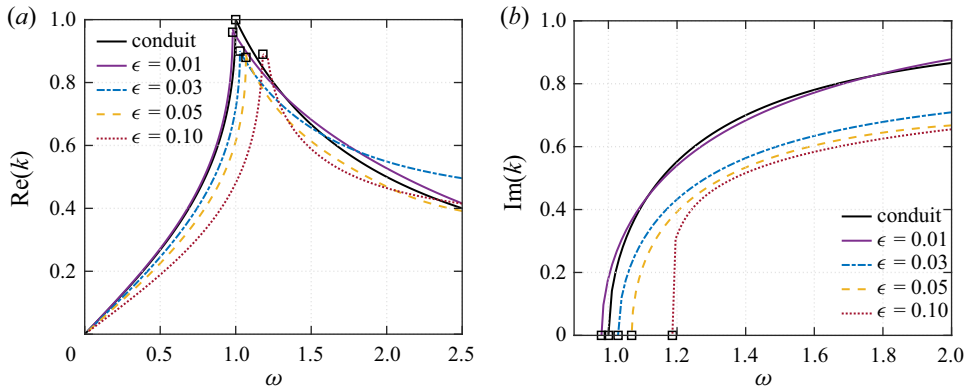
954 A14-10

Figure 3. Two-Stokes recirculating flow dispersion relation with $D/\eta = 10$, λ in (2.11) and different ϵ. Black squares represent the critical frequency ω_{cr}. (*a*) Real part of the dispersion relation $\mathrm{Re}(k(\omega))$. (*b*) Imaginary part $\mathrm{Im}(k(\omega))$.

further incorporating the outer wall's no-slip boundary condition so that

$$D = \epsilon^{-1/2}d, \quad d = O(1). \tag{2.15a,b}$$

In this case, the corresponding external pressure gradient (2.11) becomes

$$\lambda = \frac{16\epsilon \left(d^2 + 8\epsilon(\ln(8\epsilon) - 2\ln(d)) - 8\epsilon\right)}{\left(d^2 - 8\epsilon\right)^2} = \epsilon \frac{16}{d^2} + O\left(\epsilon^2 \ln(\epsilon)\right). \tag{2.16}$$

This results in higher-order corrections to the conduit unit-mean linear dispersion relation as

$$\omega(k) = \frac{2k}{1 + k^2} + 4\epsilon \ln(1/\epsilon)\, k \frac{1 + 2k^2}{(1 + k^2)^2} + \epsilon\omega_2(k) + \dots, \tag{2.17}$$

where $\omega_2(k)$ involves a complicated expression that depends on d which can be found in Appendix B. Following the assumptions of high viscosity contrast and long wavelengths, the conduit linear dispersion relation is obtained when $\epsilon \to 0$ in (2.17).

We provide the 3-term asymptotic expansion (2.17) to the two-Stokes linear dispersion relation because the 2-term expansion has limited applicability. For example, the absolute error in the wave frequency for $0 < \omega < \omega_{cr}$ between (2.17) and the full dispersion relation in figure 4 shows that the second term does not significantly improve upon the leading-order term, even for $\epsilon \approx 10^{-6}$ but the 3-term expansion does. Nevertheless, the 2-term expansion predicts an upshift in the critical frequency $\omega_{cr} = 1 + 3\epsilon \ln(1/\epsilon)$ and the critical wavenumber $k_{cr} = 1 + \epsilon \ln(1/\epsilon)$. While the former is consistent with the numerical calculation of the full dispersion in our experimental regime where $\epsilon \ll 1$ (see figure 3), the latter is not.

3. Linear modulation theory

One of the primary techniques to analytically describe the long-time asymptotics of dispersive wave problems is modulation theory (Whitham 1974). In this section, we use modulation theory to describe slow modulations of the linear periodic wave's wavenumber for the wavemaker problem. We are able to predict the propagation of waves for a specific range of frequencies.
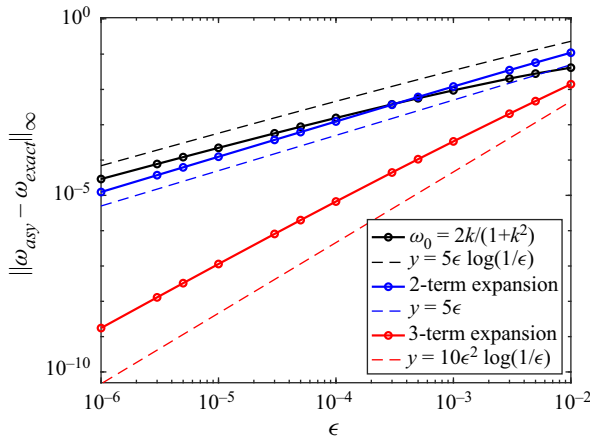
Figure 4. Maximum absolute error in the comparison of exact and asymptotic (2.17) solutions to the two-Stokes linear dispersion relation at $d = 5$.

The primary modulation equation is the conservation of waves (Whitham 1974)

$$k_t + \omega_z = 0, \tag{3.1}$$

where ω is the angular frequency and $k(\omega)$ is the local linear dispersion relation. Translating the initial-boundary value problem for $u(z, t)$ to an initial-boundary value problem for $k(z, t)$, we have

$$\left.\begin{aligned} \omega(z, 0) &= 0, \quad z \geqslant 0, \\ \omega(0, t) &= \omega_0, \quad t > 0. \end{aligned}\right\} \tag{3.2}$$

We seek a self-similar solution such that $\omega = \omega(\xi)$, $\xi = z/t$ in which $\omega'(k) = \xi$ or $d\omega/d\xi = 0$. The solution takes the form

$$\omega(\xi) = \begin{cases} \omega_0, & 0 \leqslant \xi \leqslant c_g(\omega_0) \\ g(\xi), & c_g(\omega_0) < \xi \leqslant c_g(0) \\ 0, & \xi > c_g(0) \end{cases} \tag{3.3}$$

where ω_0 is the input frequency, $c_g(\omega_0)$ represents the group velocity for the wavenumber $k_0 = k(\omega_0)$ and $g(\xi)$ is the solution to $k'(g) = 1/\xi$. Comparison between the solution (3.3) for the conduit and two-Stokes dispersion $k(\omega)$ is depicted in figure 5. In particular, the conduit equation admits a plane wave solution with constant frequency ω_0 and wavenumber $k_0 = (1 - \sqrt{1 - \omega_0^2})/\omega_0$ for $0 \leqslant \xi < \xi_0$, and a decaying oscillatory solution with $\omega(\xi) = \sqrt{1 - 2\xi + \sqrt{1 + 4\xi}}/\sqrt{2}$ and $k(\xi) = \sqrt{-1 - \xi + \sqrt{1 + 4\xi}}/\sqrt{\xi}$ for $\xi_0 \leqslant \xi \leqslant 2$. The two regions are separated by the line $\xi_0 = 1 - \omega_0^2 + \sqrt{1 - \omega_0^2}$. For the two-Stokes recirculating flow modulation solution, we have a similar profile for $\omega(\xi)$ but the group velocities $c_g(\omega_0)$, $c_g(0)$ are faster than the corresponding conduit group velocities. These calculations suggest that for an input ω_0 smaller than the critical frequency, we can generate a plane wave that will eventually propagate and fill the entire vertical conduit. We now realize this in experiments described in the next section.
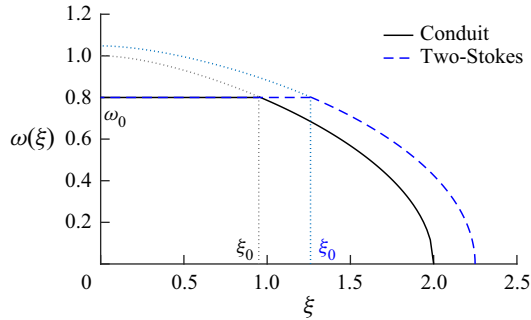
954 A14-12

Figure 5. Solution to the linear modulation equation conservation of waves with an input frequency $\omega_0 = 0.8$ for the conduit equation (black solid) and two-Stokes flow with $\epsilon = 0.04$, $D/\eta = 10$ and λ at (2.11) (blue dashed).

$\mu^{(i)}$	0.045 Pa s
$\mu^{(e)}$	1.11 Pa s
ϵ	0.041
$\rho^{(i)}$	1.21 g cm^{-3}
$\rho^{(e)}$	1.26 g cm^{-3}
Q_0	3.00 cm^3 min^{-1}
$2R_0$	0.36 cm
$2D_0$	5.00 cm
$Re^{(i)}$	0.47
$Re^{(e)}$	0.020
Camera resolution	375.60 pix cm^{-1}

Table 1. Example fluid properties measured in experiments: viscosities $\mu^{(i,e)}$, viscosity ratio ϵ, densities $\rho^{(i,e)}$, background flow rate Q_0, associated conduit diameter $2R_0$ computed by Poiseuille's law, outer wall diameter $2D_0$ and Reynolds numbers $Re^{(i,e)}$ for interior and exterior fluids.

4. Experiment

4.1. *The set-up*

The experimental set-up in figure 6(*a*) is identical to those used by Anderson *et al.* (2019) and Maiden *et al.* (2020). A conduit is formed in a square acrylic column with dimensions 5 cm × 5 cm × 180 cm. The exterior fluid is pure glycerin of high viscosity and the interior fluid consists of a miscible mixture of glycerin (∼70 %), water (∼20 %) and food colouring (∼10 %), which is less dense and less viscous than the exterior fluid. The nominal parameter values used in one of the experiments (dataset 3 in §§ 4.4, 4.5) are presented in table 1. Miscibility of the two fluids implies negligible surface tension at the interface. A free interface is sustained over the time scale of experiments because mass diffusion occurs much more slowly than momentum diffusion.

A computer-controlled piston pump is used as a wavemaker to inject the interior fluid into the extrusive fluid at the nozzle that rises buoyantly. Variation in the flow rate results in interfacial waves. Periodic waves are created by a suitable periodic injection rate $Q^{(i)}(t)$:

$$Q^{(i)}(t) = q(t), \quad t \geqslant 0, \quad q(t + T_0) = q(t), \quad T_0 = \frac{2\pi}{\omega_0}. \tag{3.4a–d}$$
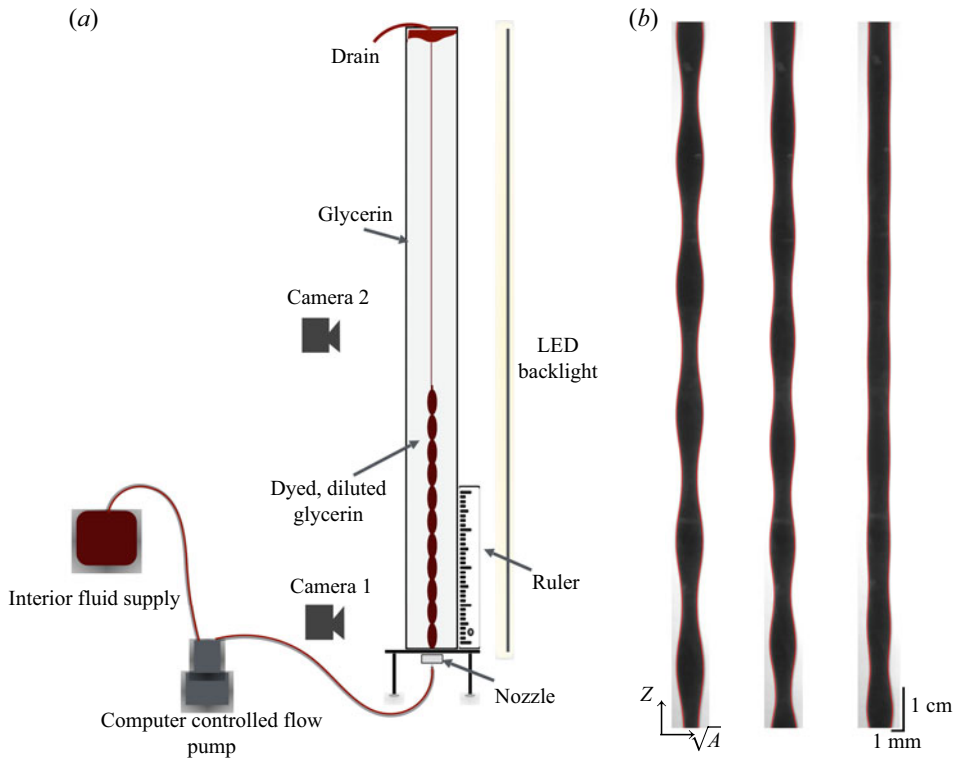
Figure 6. (*a*) Schematic of the experimental apparatus. (*b*) Waves $\omega_0 = (0.85, 0.95, 1.00)/\Omega$ with fixed amplitude $a = 0.8$ but increasing frequencies from left to right. The spatial wave is observed to be periodic in the leftmost image, but get damped in the middle and arrested in the rightmost image. Conduit edges are outlined by the red curves. Measured experimental parameters follows from table 1.

Data acquisition is performed using high-resolution cameras with one (camera 1 in figure 6*a*) equipped with a macro lens at the injection nozzle for precise data measurement and one to image the far field (camera 2) and capture fully developed periodic wavetrains. Spatial calibration is achieved with a ruler inside the column within the camera view. Example large-amplitude periodic waves generated by time-periodic boundary data with different injection frequencies and the same wave amplitude are shown in figure 6(*b*). For a relatively small frequency, the periodic wave maintains its fully developed structure, i.e. it propagates. However, by increasing the input frequency, spatial decay of the amplitude is observed. The middle wave is weakly spatially damped and the rightmost wave is arrested at a larger frequency.

4.2. *Method*

Camera images are processed to extract the conduit edges. A low-pass filter is applied to reduce noise due to pixelation of the photograph and any impurities in the exterior fluid. The conduit diameter is obtained by calculating the number of pixels between the two edges and normalizing by the conduit mean diameter. In each experimental trial, images are taken after the wave has fully developed in the camera view, and we identify $t = 0$ with the initiation of imaging. A 3 Hz sampling rate for the close camera and a 1 Hz sampling rate for the full camera were used.

954 A14-14

We present all dimensional quantities in tilde notations. The circular cross-sectional area $\tilde{A}$ of the conduit is then modelled by the dimensional conduit equation

$$\tilde{A}_{\tilde{t}} + \frac{g\Delta}{8\pi\mu^{(i)}}\left(\tilde{A}^2\right)_{\tilde{z}} - \frac{\mu^{(e)}}{8\pi\mu^{(i)}}\left(\tilde{A}^2\left(\tilde{A}^{-1}\tilde{A}_{\tilde{t}}\right)_{\tilde{z}}\right)_{\tilde{z}} = 0, \tag{4.5}$$

where $\tilde{z}, \tilde{t}$ follow from (2.6) and $\tilde{A} = \pi R_0^2 A$. Profile measurements of linear waves are conducted by scaling the data to unit mean and fitting at every temporal and spatial snapshot a sinusoidal plane wave

$$A(\tilde{z}, \tilde{t}) = 1 + \frac{a}{2}\cos(\tilde{k}\tilde{z} - \tilde{\omega}\tilde{t} + \psi), \tag{4.6}$$

where ψ represents the phase. The relative L^2 norm error in the fit is below 15 % in space and 10 % in time. To extract the wavenumber for a trial, we compute the mean of $\tilde{k}$ across a range of times $\tilde{t}$; similarly, the angular frequency is obtained by averaging $\tilde{\omega}$ over a range of heights $\tilde{z}$. The standard error in parameter measurements is roughly as low as 1 % for $\tilde{k}$ and 0.5 % for $\tilde{\omega}$, indicating that the fit (4.6) to the data results in a reliable and accurate measurement of linear periodic waves. However, this method is not suitable for waves beyond the linear regime. Instead, larger-amplitude waves with macroscopic edge changes are processed by directly splitting the waves into periods at each snapshot and computing the averaged wavelengths and wave periods. The standard error for $\tilde{k}, \tilde{\omega}$ measurements with this technique is typically below 5 %.

To compare the experimental results with theory, we require the vertical length, velocity and time scales $L, U, T = L/U$ in (2.7a–d) for non-dimensionlization. Upon generation of linear periodic waves, we non-dimensionalize the wavenumber and angular frequency data by using two fitting methods: one is to determine L_c and U_c by fitting the dimensional data $\tilde{\omega}, \tilde{k}$ to the conduit linear dispersion relation

$$f(\tilde{k}) = \frac{2U_c\tilde{k}}{1 + L_c^2\tilde{k}^2}, \tag{4.7}$$

and the other is by fitting $\tilde{\omega}, \tilde{k}$ with the two-Stokes linear dispersion relation using the spatial L_S and velocity U_S scales, as well as ϵ, λ and D. Treating ϵ, λ and D as effective fitting parameters, the two-Stokes linear dispersion relation is determined and fitted to experiments. We note that the fitting method is sensitive to the initial guess for the fitting parameters. These two techniques, which construct a direct relationship between experimental data and theory, return reliable approximations of the dimensional scaling coefficients L and U. Differences in the two methods will be discussed in § 4.4. The scales in our experiments from either fitting approach are typically in the range

$$L : 0.3\text{–}0.4 \text{ cm}, \quad U : 0.3\text{–}0.4 \text{ cm s}^{-1}, \tag{4.8a,b}$$

with camera resolutions of $250-400$ pixel cm^{-1}. Although L scales like $R_0/\sqrt{\epsilon}$ for modelling long-wavelength wave dynamics, in our experimental regime, it is comparable to the conduit diameter $2R_0$. Nevertheless, for wavenumbers $0 < k \lesssim 1$, the wavelengths are on the centimetre scale while the conduit diameter is on the scale of millimetres. Prior to each experiment described below, around 10 trials of linear periodic waves were generated for calibrating L and U according to the method described here.
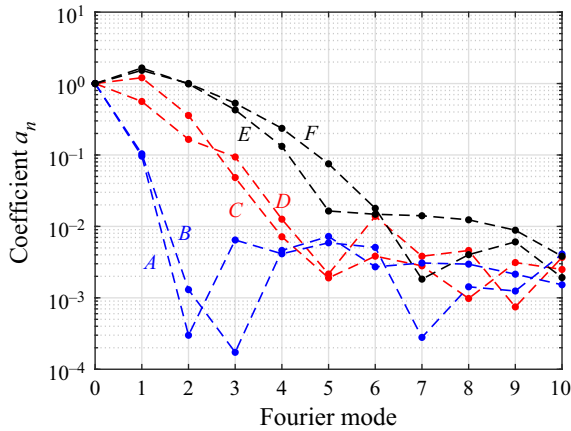
Figure 7. Fourier mode of typical periodic waves in experiments. Waves A, B with dominant a_1 can be approximated by a single sine wave. To describe larger-amplitude waves C, D, higher-harmonic terms are needed. Waves E, F with the largest amplitudes acquire non-negligible Fourier modes even at the fourth or fifth order.

4.3. *Definition of linear, weakly nonlinear and fully nonlinear regimes*

To categorize the periodic travelling waves obtained in experiments, we perform a preliminary analysis by expressing the spatial waves as a Fourier series at a fixed time $t = t_0$

$$A(z, t_0) = a_0 + \sum_{n=1}^{\infty} \frac{a_n}{2} \cos(nk(z - \psi)), \tag{4.9}$$

where $a_0 = 1$ is the wave mean. Dividing the periodic travelling wave data into periods and applying the Fourier cosine transform, we obtain the Fourier components a_n. Fourier components of some selected periodic waves are plotted in figure 7. Waves with negligible second-order and higher modes $|a_n| \ll 0.1$, $n = 2, 3, \ldots$ are identified as lying in the linear regime and can be well described by linear theory. For larger-amplitude waves ($|a_1| \gtrsim 0.5$, $|a_2| \gtrsim 0.1$), a single harmonic is insufficient and higher-order harmonic terms are needed. A clear distinction between weakly nonlinear and strongly nonlinear waves occurs when the fourth-order coefficient is sufficiently large. The waves with modes $|a_4| \lesssim 0.1$ are considered to be in the weakly nonlinear regime. On the other hand, the waves with $|a_4| \gtrsim 0.1$ are in the strongly nonlinear regime, in which case the weakly nonlinear approximation of three harmonics fails. We now assess each wave class beginning with linear waves.

4.4. *Linear periodic travelling waves*

An example linear periodic travelling wave launched in a viscous fluid conduit by the sinusoidal boundary condition $Q(\tilde{t}) = Q_0(1 + (a/2) \cos(\tilde{\omega}\tilde{t} + \pi/2))^2$ for $\tilde{t} > 0$ is depicted in figure 8(*a*). The wave travelling in the positive $\tilde{z}$ direction is periodic in both time and space. Extracting the spatial wave at a fixed time, we fit the periodic wave with a cosine function in figure 8(*b*). A movie of the linear periodic wave propagation can be found in the supplementary material. This result confirms the prediction from modulation theory that a fully developed periodic wave is generated for input frequency less than the critical value (see (1.11) and (3.3)). Three independent experiments with different fluid properties
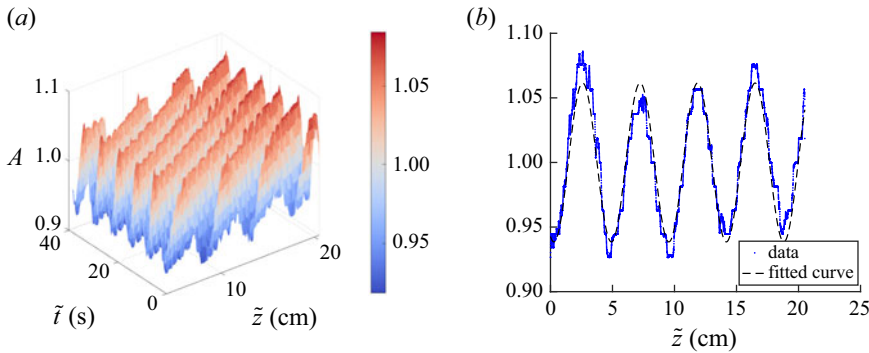
954 A14-16

Figure 8. (*a*) Example experimental data of a linear periodic travelling wave in the viscous fluid conduit. Measured wave parameters are $a = 0.12$, $\tilde{k} = 1.34 \pm 0.04$ rad cm^{-1} and $\tilde{\omega} = 0.86 \pm 0.01$ rad s^{-1}. (*b*) Linear wave data in the spatial domain at $\tilde{t} = 39$ s fitted with a sinusoidal waveform. The non-dimensionalization scales are $L = 0.35 \pm 0.01$ cm and $U = 0.39 \pm 0.01$ cm s^{-1}.

resulting in three datasets of measured wavenumbers $\tilde{k}$ and wave frequencies $\tilde{\omega}$ were collected. In figure 9, we compare the dimensionless experimental observations of $k(\omega)$ with the conduit linear dispersion relation (1.11). Across all three datasets, good agreement between the experimental data and the theoretical prediction is achieved for sufficiently long wavelengths $\tilde{\zeta} = (2\pi/k)L_c \gtrsim 2.3$ cm ($k < 0.8$). The linear dispersion relation of the conduit equation is quantitatively verified in this regime. However, the experimental critical frequency ω_{cr} and critical wavenumber k_{cr} corresponding to the values between the last datapoint of each dataset in figure 9 and the first point where the wave is damped are subject to a significant shift from 1, the prediction from the conduit equation. The relative discrepancies in ω_{cr} and k_{cr} are $(\Delta\omega_{cr}, \Delta k_{cr}) = (5\,\%, 27\,\%), (7\,\%, 33\,\%), (6\,\%, 29\,\%)$, respectively. It is notable that the observed critical frequency and wavenumber vary across the three datasets where the fluid properties differ. The interior flow rate is calculated using Poiseuille's law and (2.7*a*–*d*) for a motionless external fluid so that $Q^{(i)} = \pi U R_0^2$, where $U = U_c$ is the fitted velocity scale and R_0 is the conduit radius measured from experiments. Datasets 1–3 have measured radii $R_0 = 0.19, 0.17, 0.18$ cm. As expected for the asymptotic validity of the conduit equation, the vertical wavelength is much larger than the horizontal diameter, i.e. $\tilde{\zeta} \gg 2R_0$. We obtain $Q^{(i)} = 2.7, 1.7, 2.5$ ml min^{-1} for each dataset compared with the nominal input flow rates $Q_0 = 3.0 \pm 0.1, 2.0 \pm 0.1, 3.0 \pm 0.1$ ml min^{-1}, respectively.

To further interpret the linear periodic waves obtained in experiments and investigate the shorter-wave regime in the neighbourhood of the critical frequency, we compare the experimental results with the linear dispersion relation for two-Stokes interfacial waves (2.14) subject to the assumption $Q^{(e)} = 0$ in (2.9*b*) so that λ follows from (2.11). We fit the experimental data $\tilde{k}(\tilde{\omega})$ in the subcritical regime with the two-Stokes dispersion relation using effective fitting parameters ϵ, D, as well as the scales L_S and U_S to give an exactly matched critical frequency ω_{cr}. Each dataset was collected independently and therefore possesses distinct fluid parameters, although they are all similar. Figure 10 shows the fits and table 2 reports the corresponding ω_{cr} and k_{cr}. It is demonstrated that this fitting procedure results in an upshift in the critical frequency and a downshift in the critical wavenumber. Two-Stokes linear dispersion curves well describe the dispersion relation $k(\omega)$ and provide improved predictions for the critical values. Errors in the critical wavenumber k_{cr} are caused by the step size of the input ω in experiments, the sensitivity
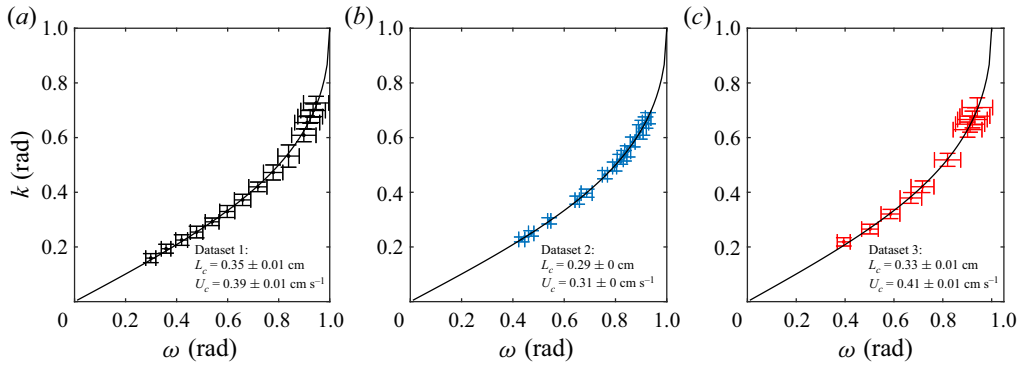
Figure 9. Fit of the experimental measurements $k(\omega)$ (dots) to the conduit linear dispersion relation (black curve). Error bars take account of the errors in measurements using (4.6) and errors in non-dimensionalization.
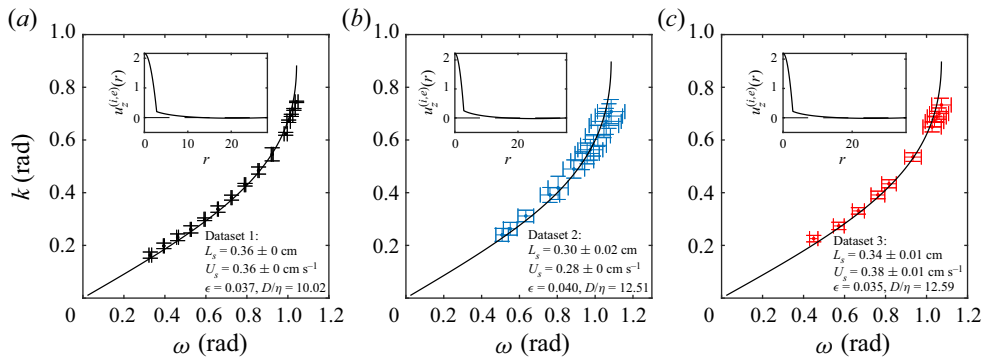

Figure 10. Experimental results of linear periodic waves $k(\omega)$ (dots) fitted with the two-Stokes dispersion relation assuming (2.11) (black curve). Insets report predicted recirculating vertical flow velocities.

of k_{cr} on fluid parameters and limitations in the fitting method. As ω approaches ω_{cr}, $k'(\omega) \to \infty$ so that a small change in ω will lead to a substantial difference in k, leading to difficulties in approximating k_{cr}. The predicted interior flow rates from the fits using (2.9a) for dataset 1 to 3 are $Q^{(i)} = 3.1, 1.9, 2.7$ ml min^{-1}, reasonably consistent with the input $Q_0 = 3.0, 2.0, 3.0$ ml min^{-1}, and the predicted interior radii obtained from (2.7a–d) are $R_0 = 0.20, 0.17, 0.18$ cm, respectively. The two-Stokes dispersion relation follows from the physical scenario that we observed in experiments where the interior fluid flows up and pools at the top over time while the exterior flow recirculates with a zero net flow rate.

We have shown that the two-Stokes recirculating flow that includes an external fluid pressure gradient and exterior flow mass conservation is a slightly more accurate model of propagating linear waves generated by a wavemaker than the long-wave conduit equation for describing relatively short waves between two viscous fluids in the linear regime. It is notable, however, that the conduit equation accurately reproduces the subcritical data.

4.5. *Linear wave damping and arresting*

Linear periodic waves in the short-wave, supercritical regime when the injection frequency ω exceeds the critical frequency ω_{cr} exhibit spatial amplitude damping and do not propagate unhindered. Figures 11(a) and 11(b) demonstrate an example of a damped wave

954 A14-18

| Dataset | Measured | | Two Stokes | | Relative error |
	ω_{cr}	k_{cr}	ω_{cr}	k_{cr}	Δk_{cr}
01	1.04 ± 0.01	0.75 ± 0.01	1.04	0.88	15 %
02	1.08 ± 0.07	0.71 ± 0.05	1.08	0.90	21 %
03	1.07 ± 0.05	0.73 ± 0.03	1.07	0.90	19 %

Table 2. Comparison of ω_{cr} and k_{cr} between experimental measurements and the two-Stokes linear dispersion relation assuming (2.11) (fittings are reported in figure 10). The fitting method requires an exactly correct ω_{cr}. Δk_{cr} reports the relative difference of k_{cr}.
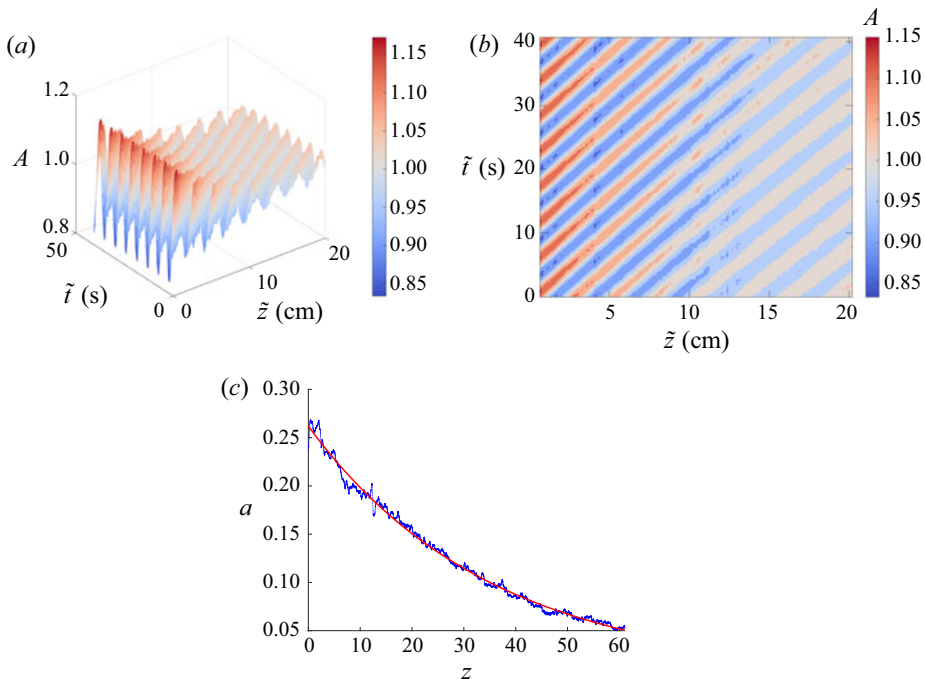

Figure 11. (*a*) Surface and (*b*) contour plots of an experimental small-amplitude, damped, non-propagating wave when the injection frequency at the boundary exceeds the critical value. Dimensional wave parameters are $\tilde{\omega} = 1.12 \pm 0.03$ rad s^{-1} and $\tilde{k} = 2.32 \pm 0.04$ rad cm^{-1} with scales $L = 0.35 \pm 0.01$ cm, $U = 0.40 \pm 0.01$ cm s^{-1}. (*c*) Amplitude decay (dotted blue) fitted with $a \exp(-bz)$, $a = 0.26 \pm 0.01$, $b = 0.027 \pm 0.001$ (solid red).

observed in a viscous fluid conduit (see the supplementary material for movies). The wave generated by a time-harmonic injection rate at the nozzle quickly decays spatially while maintaining periodicity in time at each fixed spatial location. By measuring the spatial dependence of the amplitude of the wave in figure 11(*c*), we find that it is well fitted by an exponential function in space. This agrees with our hypothesis derived from the radiation condition (1.11) so that for complex dispersion $k = k_{Re} + ik_{Im}$, the plane wave solution takes the form

$$A(z, t) = a \exp(-k_{Im}z) \cos(k_{Re}z + \omega t + \psi), \qquad (4.10)$$

where k_{Im} is the spatial damping rate and $k = k(\omega)$ is obtained from the linear dispersion relation in the supercritical regime.
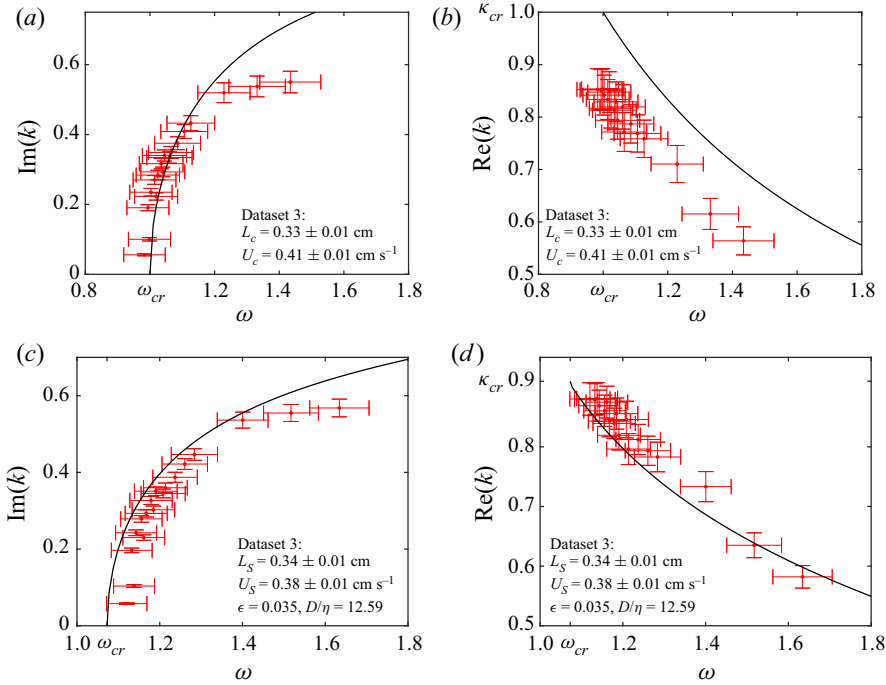
Figure 12. Comparison between experimental measurements (red dots) of the exponential spatial decay rate (*a,c*), spatial frequency (*b,d*) and theory (black line) for waves in the supercritical regime $\omega > \omega_{cr}$. (*a,c*) The conduit linear dispersion relation. (*b,d*) The two-Stokes dispersion relation.

The exact linear dispersion relation of the conduit equation and the two-Stokes flow system obtained in § 2 are used to compare with the experimental wave profiles. Here, we report the data points in figure 12 as collected using the same experimental set-up as those in figures 9(*c*) and 10(*c*); therefore, identical parameters and non-dimensionalization scales are used. No new fitting is applied. For a total of 18 experimental trials, k_{Im} is obtained as the spatial amplitude damping rate by fitting an exponential to the wave amplitude, ω is the averaged frequency over a spatial window size of $z \in [0, 2] \to [0, 0.7$ cm] (250 data points) measured through the cosine fitting method described in § 4.2, and k_{Re} is the slope of the temporal wave phase over the same spatial window. Figure 12 reports the comparison of the linear dispersion relation in the supercritical regime from experiments and theory. It is shown that the experimental results closely match the two-Stokes theoretical predictions and the first data point of the damping wave is also well approximated by the two-Stokes predicted ω_{cr}, k_{cr}. The conduit dispersion relation also performs well at describing k_{Im} but significantly overshoots k_{Re}.

Damped waves are found to exhibit a spatially dependent frequency and wavenumber, as shown in figure 13. Through temporal data fitting with the function $\phi(t) = a \cos(-\omega t + \psi)$, we obtain the amplitude a, frequency ω and phase ψ, whose slope is the real part of the local wavenumber k_{Re}. The amplitude fits well to an exponential $\propto e^{-k_{Im}z}$ that is consistent with linear theory. Additionally, the local temporal ω and spatial k_{Re} frequencies are also observed to spatially decrease, which we suspect to be a nonlinear effect.

Nevertheless, the conduit equation again provides a reasonable description of part of the supercritical data. We now focus solely on the conduit equation to model nonlinear waves.
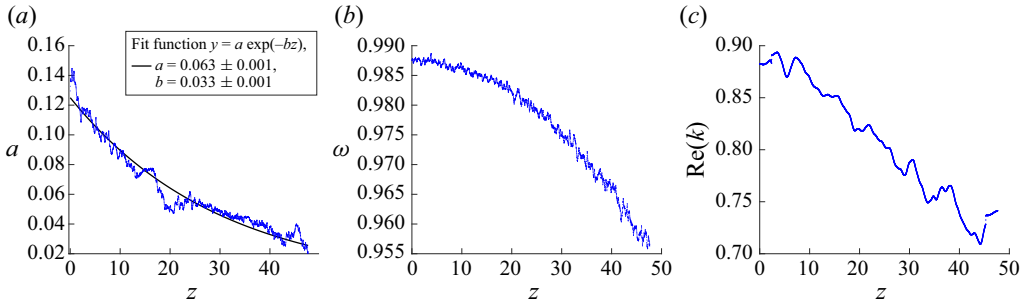
954 A14-20

Figure 13. Investigation of a spatially damped wave profile. (*a*) The amplitude decay is fitted with an exponential function. The decay rate b is equivalent to k_{Im} in (4.10). (*b*) The frequency is also found to slightly decrease ($\sim 3\,\%$) in space. (*c*) The real part of the wavenumber is subject to a decay of $\sim 20\,\%$ in space.

4.6. *Periodic travelling waves in the weakly nonlinear regime*

Larger-amplitude, periodic travelling waves in the weakly nonlinear regime are distinguished from their linear counterpart by no longer maintaining symmetry about the wave mean and cannot be described by a single trigonometric harmonic. The waves are more accurately modelled by the weakly nonlinear approximation (1.14*a*), (1.14*b*) of the conduit equation obtained via the amplitude expansions $\phi \sim 1 + a\phi_1 + a^2\phi_2 + a^3\phi_3$ and $k \sim k_0 + a^2 k_1$, where $0 < a \ll 1$ is an amplitude scale. An experimental weakly nonlinear wave is shown in figure 14. Length and velocity scales for non-dimensionalization are $(L_c, U_c) = (0.33 \pm 0.01\ \mathrm{cm}, 0.38 \pm 0.01\ \mathrm{cm\ s^{-1}})$. The dimensional spatial wave in figure 14(*a*) is fitted with the three harmonic expansion (1.13) at $\tilde{t} = \tilde{t}_0$

$$\phi(\tilde{z}) = 1 + \frac{a_z}{2}\cos(\tilde{k}\tilde{z} + \psi_1) + \frac{1 + \tilde{k}^2}{48\tilde{k}^2}a_z^2 \cos(2(\tilde{k}\tilde{z} + \psi_1)) + \frac{1 + \tilde{k}^2}{1536\tilde{k}^4}a_z^3 \cos(3(\tilde{k}\tilde{z} + \psi_1)),$$

(4.11)

where $a_z = 1.10 \pm 0.01$, $k = 0.50 \pm 0.01$ ($\tilde{k} = 1.52 \pm 0.01$ rad cm^{-1}) and $\psi_1 = 2.05 \pm 0.01$. The approximate frequency is derived from figure 14(*c*), where the dimensional temporal wave is approximated by (1.14*a*) at $\tilde{z} = \tilde{z}_0$

$$\phi(\tilde{t}) = 1 + \frac{a_t}{2}\cos(\tilde{\omega}\tilde{t} + \psi_2) + \frac{a_t^2}{24\left(1 - \sqrt{1 - \tilde{\omega}^2}\right)}\cos(2(\tilde{\omega}\tilde{t} + \psi_2))$$

$$+ \frac{\left(-1 - \sqrt{1 - \tilde{\omega}^2}\right)a_t^3}{768\left(-2 + \tilde{\omega}^2 + 2\sqrt{1 - \tilde{\omega}^2}\right)}\cos(3(\tilde{\omega}\tilde{t} + \psi_2)),$$

(4.12)

with $a_t = 1.06 \pm 0.02$, $\omega = 0.78 \pm 0.01$ ($\tilde{\omega} = 0.90 \pm 0.01$ rad s^{-1}) and $\psi_2 = -2.97 \pm 0.03$. The fits exhibit a maximum absolute error of 0.11 and have larger discrepancies at the wave peaks. Adding higher-order harmonic terms yield an even better approximation.

A total of 11 trials were measured in the weakly nonlinear regime with the same input amplitude and various input frequencies. Wave profiles are measured as follows. Fitting the spatial and temporal waves with the weakly nonlinear expansions (4.11), (4.12), we obtain dimensionless $k = \tilde{k}L$, $\omega = \tilde{\omega}(L/U)$ as well as $a = (a_z + a_t)/2$ for those 11 trials as the red circles in figure 15. Experimental results are then compared with the weakly nonlinear dispersion relation (1.14*b*) and the linear dispersion relation
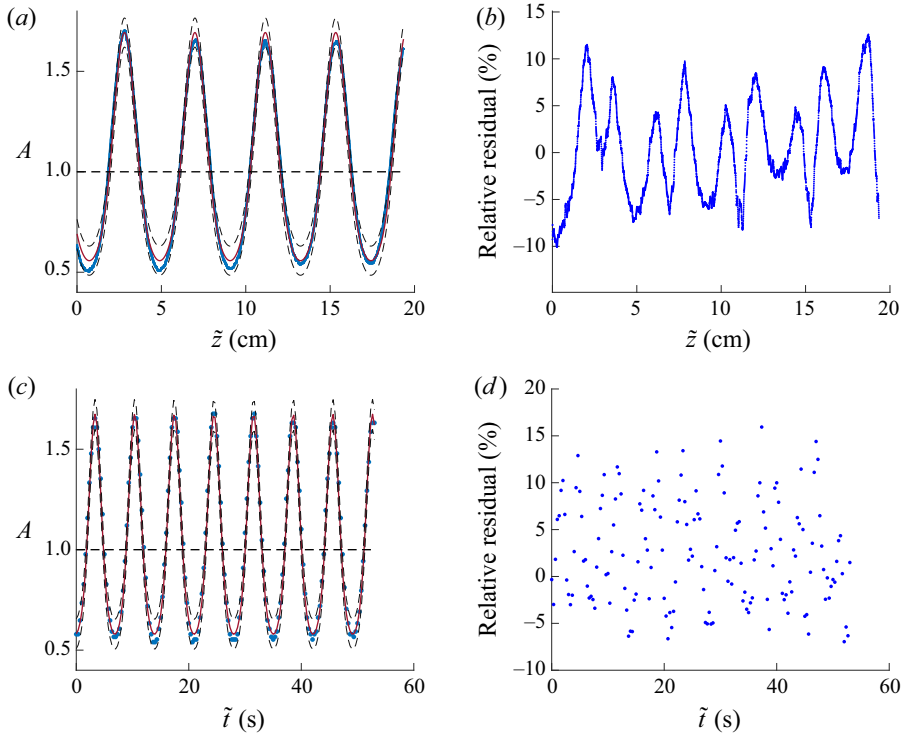
Figure 14. Measured periodic waves (blue dots) and the weakly nonlinear approximation (red solid lines). Error bars are represented by grey dashed lines and the horizontal black dashed line is the wave mean. (*a*) The spatial wave at a fixed $\tilde{t}$ fitted with expansion (4.11). (*b*) Percentage relative error in space. (*c*) Wave in the time domain at a fixed $\tilde{z}$ fitted with expansion (4.12). (*d*) Percentage relative error in time.

(1.10) in figure 15. Although weak nonlinearity does not lead to a significant deviation from the linear dispersion relation, we have shown that the corresponding wave profiles require amplitude-dependent higher harmonics to quantitatively model the experimental observations. We have quantitatively validated the weakly nonlinear approximation for measured conduit periodic travelling waves of sufficiently large amplitude and demonstrated the necessity of including higher-order harmonic terms in this regime.

4.7. *Cnoidal-like nonlinear periodic waves*

We now investigate periodic travelling waves with large amplitudes in the fully nonlinear regime (see the supplementary material for movies). We refer to these waves as cnoidal like, owing to their similarities to the KdV/BBM cnoidal wave solutions (1.5). First, we generate linear periodic waves for calibrating the scales $L_c = 0.26 \pm 0.01$ cm and $U_c = 0.25 \pm 0.01$ cm s^{-1}. We then utilize a numerical database of pre-computed conduit cnoidal-like solutions (Maiden & Hoefer 2016) to experimentally generate and analyse the observed large-amplitude periodic waves. Waves are generated by varying the injection flow rate according to

$$Q(\tilde{t}) = Q_0 \phi^2(-\tilde{\omega}\tilde{t}), \tag{4.13}$$

where ϕ is a cnoidal-like solution with unit mean satisfying (1.9). Measured waves are processed by dividing each space and time window into spatial and temporal periods.
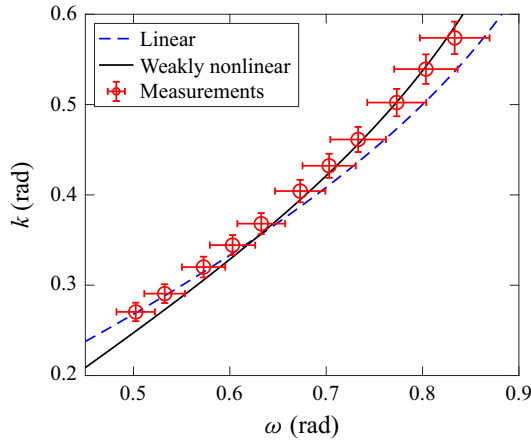
Figure 15. Non-dimensional experimental wave profiles $k(\omega)$ (circles) compared with the weakly nonlinear dispersion relation (1.14*b*) at $a = 1.04$ (black solid line) and the linear dispersion relation (blue dashed line).

The average of all processed periods and wave profiles are then reported. Figure 16 displays two example wave profiles, separately in space and time. By direct comparison, it is clear that the observed large-amplitude waves cannot be described by linear or weakly nonlinear approximations. Instead, we compare the observed waves with cnoidal-like solutions to the conduit equation. The amplitude is obtained as $a_z = \max(\phi(z)) - \min(\phi(z))$ for waves in the spatial domain, and $a_t = \max(\phi(t)) - \min(\phi(t))$ for waves in the temporal domain. Here, ω and k are measured by the relation $\omega = 2\pi/\overline{T_0}$, $k = 2\pi/\bar{\zeta}$ with non-dimensional averaged time period $\overline{T_0}$ and averaged wavelength $\bar{\zeta}$. The set of unit-mean cnoidal-like solutions is a two-parameter family. Taking (a_z, k) as the parameters for spatial waves and (a_t, ω) as the parameters for temporal waves, the corresponding cnoidal-like solutions are compared with the experiments in figure 16. The cnoidal-like wave profiles are barely distinguishable from the observed wave profiles. We stress that we have not performed any fitting in this procedure other than the independent determination of the scales L_c and U_c from linear wave dispersion measurements. The cnoidal-like solution of the conduit equation is uniquely selected from the two-parameter family using the extracted (a_z, k) in the spatial case or (a_t, ω) in the temporal case. No profile fitting was performed. However, discrepancies in spatial and temporal profile measurements lead to (a_z, k) and (a_t, ω) belonging to two slightly different cnoidal-like solutions for the same trial. We report the average of the two amplitudes $a_{avg} = (a_z + a_t)/2$ in table 3. To see how close the solutions are, measurements of wave parameters for 15 trials are reported in table 3 and figure 17.

The nonlinear dispersion relation $k(\omega, a_{avg})$ is compared between experiments and cnoidal-like solutions in figure 17. Agreement is quantitatively achieved for all but three trials within 5 % relative error, with at most 10 % error otherwise. These measurements are across a range of wave amplitudes $a_{avg} \in (0.89, 2.2)$ and frequencies $\omega \in (0.44, 0.62)$. The trials in figure 17 are numbered from highest amplitude to lowest, as shown in table 3. Notably, the experimentally measured wavenumbers exceed the predicted values across all 15 trials. Although a different class of waves, we remark that previous measurements of large-amplitude soliton solutions in Olson & Christensen (1986) found that the soliton speed was consistently underpredicted by conduit equation soliton solutions. We hypothesize that inclusion of the weakly recirculating flow in the model could improve upon the already good predictions.
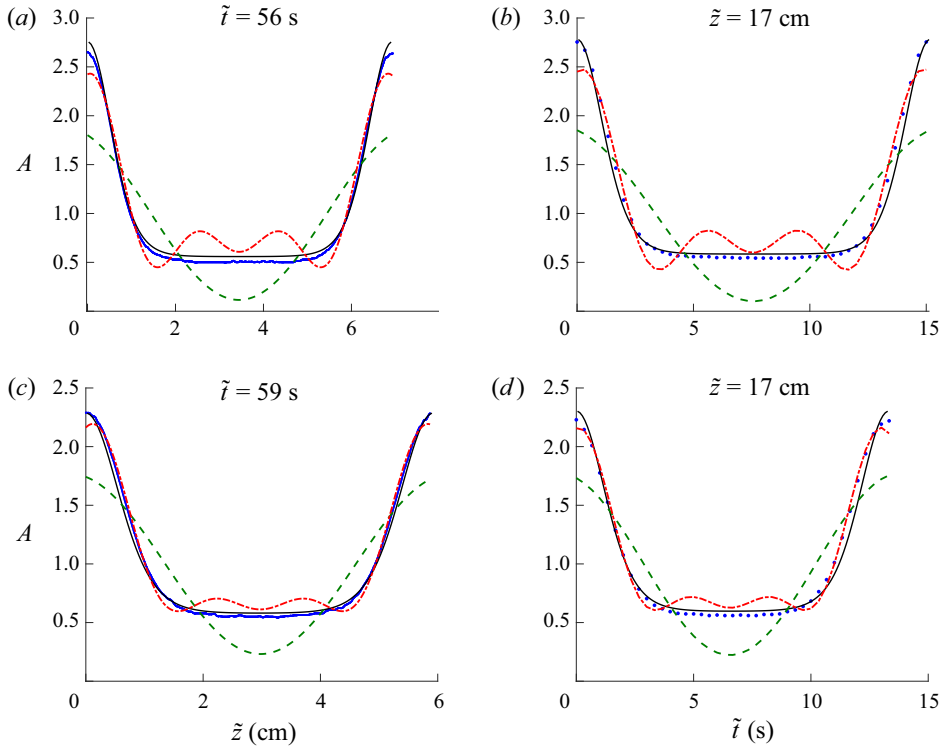
Figure 16. Averaged experimental wave profiles over one wavelength or period (blue dots) compared with linear (green dashed), weakly nonlinear (red dash-dotted) approximations and cnoidal-like solutions (black solid) in both spatial (*a*,*c*) and temporal (*b*,*d*) domains. (*a*,*b*) The extracted wave parameters are $(a_{avg}, \omega, k) = (2.20, 0.44, 0.24)$ (trial 1 in figure 17). (*c*,*d*) The extracted parameters are $(a_{avg}, \omega, k) = (1.71, 0.50, 0.28)$ (trial 3 in figure 17).
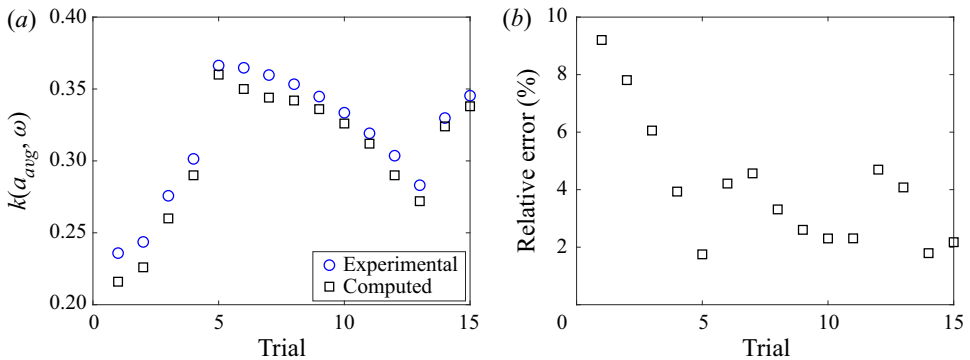
Figure 17. (*a*) Comparison of the conduit equation nonlinear dispersion relation for cnoidal-like solutions. Data points are from the trials reported in table 3. Utilizing measured (a_{avg}, ω) as the parameters, experimental wavenumbers (blue circles) are compared with the numerically computed nonlinear dispersion relation $k(a_{avg}, \omega)$ (black squares). (*b*) Percentage relative error in *k* for each trial.

954 A14-24

Trial	a_{avg}	ω(rad)	k(rad)	$k(a_{avg}, \omega)$	Relative error in k
01	2.20 ± 0.03	0.44 ± 0.02	0.24 ± 0.01	0.22	9 %
02	2.13 ± 0.01	0.45 ± 0.02	0.24 ± 0.01	0.23	8 %
03	1.71 ± 0.01	0.50 ± 0.01	0.28 ± 0.01	0.26	6 %
04	1.42 ± 0.01	0.54 ± 0.01	0.30 ± 0.01	0.29	4 %
05	1.30 ± 0.01	0.62 ± 0.02	0.37 ± 0.01	0.36	2 %
06	1.27 ± 0.01	0.61 ± 0.03	0.36 ± 0.01	0.35	4 %
07	1.26 ± 0.01	0.61 ± 0.02	0.36 ± 0.01	0.34	5 %
08	1.25 ± 0.01	0.60 ± 0.01	0.35 ± 0.01	0.34	3 %
09	1.24 ± 0.01	0.60 ± 0.03	0.34 ± 0.01	0.34	3 %
10	1.23 ± 0.01	0.59 ± 0.01	0.33 ± 0.01	0.33	2 %
11	1.22 ± 0.01	0.57 ± 0.01	0.32 ± 0.01	0.31	2 %
12	1.18 ± 0.01	0.54 ± 0.02	0.30 ± 0.01	0.29	5 %
13	1.15 ± 0.01	0.52 ± 0.02	0.28 ± 0.01	0.27	4 %
14	1.09 ± 0.01	0.59 ± 0.01	0.33 ± 0.01	0.32	2 %
15	0.89 ± 0.01	0.60 ± 0.01	0.35 ± 0.01	0.34	2 %

Table 3. Nonlinear periodic wave measurements. Columns 2–4: measured wave parameters. Column 5: numerically computed solution k at measured (a_{avg}, ω). Column 6: relative error between experimental k and cnoidal-like wave solutions. Trials 1 and 3 are depicted in figure 16. All trials are shown in figure 17.

5. Discussion and conclusion

The main result of this study is the reliable generation of periodic travelling waves in a viscous fluid conduit across a wide range of amplitudes and long to short wavelengths that are well modelled by the conduit equation. This provides further evidence of the viscous fluid conduit as an accessible and flexible laboratory system for the study of nonlinear wave dynamics with an accurate partial differential equation model in the conduit equation. In order to quantitatively model shorter small-amplitude waves, we found it helpful to derive the full two-Stokes linear dispersion relation that accounts for the actual conditions in our experiment. Radial variation in the vertical velocity allows for a non-negligible exterior pressure gradient and recirculating flow. Together with an outer wall, these two main factors give rise to an upshifted critical frequency for the transition from propagating to non-propagating, spatially damped waves. This upshift from the conduit equation's critical frequency in the short-wave regime is observed and verified quantitatively. The two-Stokes recirculating flow system with exterior flow mass conservation is therefore considered to be a more precise model in which we successfully extend the linear dispersive properties of the model to a shorter-wave regime. The two-Stokes linear dispersion relation is exactly obtained in terms of Bessel functions. Nevertheless, the conduit equation remains an excellent model of propagating linear waves.

Another key result of this experimental investigation is the existence and stability of periodic travelling waves in the fluid conduit wavemaker problem. Low-frequency periodic waves generated at the boundary with a time-periodic injection rate are observed to coherently propagate as travelling waves. Arrested wave propagation for waves generated above the critical injection frequency was observed and found to quantitatively match the two-Stokes dispersion relation for real frequencies and complex wavenumbers. These observations are explained in terms of the radiation condition and linear wave modulation theory.

In addition to presenting a careful analysis of linear periodic waves, our work also contributes to an understanding of conduit periodic travelling waves in the weakly nonlinear and strongly nonlinear regimes. Nonlinear periodic waves are found

to require more Fourier harmonics with strongly nonlinear waves well described by cnoidal-like solutions of the conduit equation. Quantitative agreement is achieved between experimental results and conduit cnoidal-like solutions for both the nonlinear dispersion relation and the wave profiles. The characterization of strongly nonlinear periodic travelling waves and their reliable generation in a viscous fluid conduit hold promise for future studies of more general boundary value problems in dispersive hydrodynamics (El & Hoefer 2016), including the generalized Riemann problem and the generation of breathers and breather trains.

Supplementary movies. Supplementary movies are available at https://doi.org/10.1017/jfm.2022.993.

Author ORCIDs.
Yifeng Mao https://orcid.org/0000-0003-1863-8945;
Mark A. Hoefer https://orcid.org/0000-0001-5883-6562.

Appendix A. Two-Stokes flow and non-dimensionalization

The governing equations (2.1a) for continuity and momentum conservation will now be non-dimensionalized according to (2.6). Equations for the interior fluid take the non-dimensional form

$$\frac{1}{r}\frac{\partial}{\partial r}(ru_r^{(i)}) + \epsilon^{1/2}\frac{\partial u_z^{(i)}}{\partial z} = 0, \tag{A1a}$$

$$-\epsilon^{-3/2}\frac{\partial p^{(i)}}{\partial r} + \nabla^2 u_r^{(i)} - \epsilon^{-1}\frac{u_r^{(i)}}{r^2} = 0, \tag{A1b}$$

$$-\epsilon^{-1}\frac{\partial p^{(i)}}{\partial z} + \nabla^2 u_z^{(i)} = 0, \tag{A1c}$$

where $\nabla^2 = \epsilon^{-1}(1/r)(\partial/\partial r)(r(\partial/\partial r)) + \partial^2/\partial z^2$. For the exterior fluid, the equations are

$$\frac{1}{r}\frac{\partial}{\partial r}(ru_r^{(e)}) + \epsilon^{1/2}\frac{\partial u_z^{(e)}}{\partial z} = 0, \tag{A2a}$$

$$-\epsilon^{-1/2}\frac{\partial p^{(e)}}{\partial r} + \nabla^2 u_r^{(e)} - \epsilon^{-1}\frac{u_r^{(e)}}{r^2} = 0, \tag{A2b}$$

$$-\frac{\partial p^{(e)}}{\partial z} + \nabla^2 u_z^{(e)} = 0. \tag{A2c}$$

The kinematic boundary condition is

$$u_r^{(i)} = \epsilon^{1/2}\left(\frac{\partial R}{\partial t} + u_z^{(i)}\frac{\partial R}{\partial z}\right), \quad r = R(z, t). \tag{A3a,b}$$

Equations for continuity of the velocity components are

$$(\mathbf{u}_r^{(i)} - u_r^{(e)}) = \epsilon^{1/2}\frac{\partial R}{\partial z}(u_z^{(i)} - u_z^{(e)}), \quad r = R(z,t), \tag{A4a}$$

$$(u_z^{(e)} - \mathbf{u}_z^{(i)}) = \epsilon^{1/2}\frac{\partial R}{\partial z}(u_r^{(i)} - u_r^{(e)}), \quad r = R(z,t). \tag{A4b}$$

The non-dimensional stress balance conditions in the normal and tangential directions are, respectively,

$$\left[-\|\mathbf{n}_c\|^2 P + \kappa\left(\sigma_{rr} - 2\epsilon^{1/2}\frac{\partial R}{\partial z}\sigma_{rz} + \epsilon\left(\frac{\partial R}{\partial z}\right)^2\sigma_{zz}\right)\right]_j = 0, \quad r = R(z,t), \tag{A5a}$$

$$\left[\kappa\left\{ -\left(1 - \epsilon\left(\frac{\partial R}{\partial z}\right)^2\right)\sigma_{rz} + \epsilon^{1/2}\frac{\partial R}{\partial z}(\sigma_{zz} - \sigma_{rr})\right\}\right]_j = 0, \quad r = R(z,t), \tag{A5b}$$

where $\kappa^{(e)} = \epsilon^{-1}, \kappa^{(i)} = 1$ are the fluid-specific coefficients, $\mathbf{n}_c = [\,_{-\epsilon^{1/2}\partial R/\partial z}^{\quad 1}\,]$ is the normal vector for the conduit and P is the scaled, absolute pressure with $P^{(i,e)} = p^{(i,e)} - \rho^{(i,e)}z/(\rho^{(e)} - \rho^{(i)})$. The normalized deviatoric stress tensor is

$$\boldsymbol{\sigma}^{(i,e)} = \begin{bmatrix} \sigma_{rr}^{(i,e)} & \sigma_{rz}^{(i,e)} \\ \sigma_{zr}^{(i,e)} & \sigma_{zz}^{(i,e)} \end{bmatrix} = \epsilon^{1/2}\begin{bmatrix} 2\dfrac{\partial u_r^{(i,e)}}{\partial r} & \dfrac{\partial u_z^{(i,e)}}{\partial r} + \epsilon^{1/2}\dfrac{\partial u_r^{(i,e)}}{\partial z} \\ \dfrac{\partial u_z^{(i,e)}}{\partial r} + \epsilon^{1/2}\dfrac{\partial u_r^{(i,e)}}{\partial z} & 2\epsilon^{1/2}\dfrac{\partial u_z^{(i,e)}}{\partial z} \end{bmatrix}. \tag{A6}$$

The above non-dimensional governing equations associated with the interfacial boundary conditions, as well as the boundary conditions along the symmetry axis $\mathbf{u}_r^{(i)} = \partial u_z^{(i)}/\partial r = \partial p^{(i)}/\partial r = 0$ at $r = 0$ and the outer wall $u_r^{(e)} = u_z^{(e)} = 0$ at $r = D$ provide a complete description of the dynamics of the two-Stokes interfacial flow.

Appendix B. Two-Stokes exact linear dispersion relation

In this section, we derive the solutions for the eigenfunctions in the two-Stokes flow linearization (2.12a)–(2.12d) and compute the exact linear dispersion relation. The differential equations for two-Stokes flow disturbances are

$$\frac{\mathrm{d}g_r(r)}{\mathrm{d}r} + \frac{g_r(r)}{r} + kg_z(r) = 0, \tag{B1a}$$

$$\epsilon g_r'' + \frac{\epsilon g_r'}{r} - k^2\epsilon^2 g_r - \frac{\epsilon g_r}{r^2} + ih'(r) = 0, \tag{B1b}$$

$$g_z'' + \frac{g_z'}{r} - k^2\epsilon g_z - ikh(r) = 0, \tag{B1c}$$

954 A14-27

for the interior fluid on the interval $0 \leqslant r \leqslant \eta$ and

$$\frac{\mathrm{d}G_r(r)}{\mathrm{d}r} + \frac{G_r(r)}{r} + k\epsilon G_z(r) = 0, \tag{B2a}$$

$$G_r'' + \frac{G_r'}{r} - k^2\epsilon G_r - \frac{G_r}{r^2} + iH'(r) = 0, \tag{B2b}$$

$$G_z'' + \frac{G_z'}{r} - k^2\epsilon G_z - ikH(r) = 0, \tag{B2c}$$

for the exterior fluid on the interval $\eta \leqslant r \leqslant D$. Along with the interfacial boundary conditions expanded about $r = R(z,t) = \eta + a\exp(i(kz - \omega t))$

$$ku_{z,0}^{(i)}(\eta) - g_r(\eta) - \omega = 0, \tag{B3a}$$

$$\epsilon ku_{z,0}^{(e)}(\eta) - ku_{z,0}^{(i)}(\eta) + g_r(\eta) - G_r(\eta) = 0, \tag{B3b}$$

$$\epsilon \frac{\partial u_{z,0}^{(e)}}{\partial r}(\eta) - \frac{\partial u_{z,0}^{(i)}}{\partial r}(\eta) - g_z(\eta) + \epsilon G_z(\eta) = 0, \tag{B3c}$$

$$-2i\epsilon k\frac{\partial u_{z,0}^{(e)}}{\partial r}(\eta) + 2i\epsilon k\frac{\partial u_{z,0}^{(i)}}{\partial r}(\eta) - 2i\epsilon g_r'(\eta) + 2iG_r'(\eta) + h(\eta) - \epsilon H(\eta) = 0, \tag{B3d}$$

$$-\frac{\partial^2 u_{z,0}^{(e)}}{\partial r^2}(\eta) + \frac{\partial^2 u_{z,0}^{(i)}}{\partial r^2}(\eta) - \epsilon kg_r(\eta) + kG_r(\eta) + g_z'(\eta) - G_z'(\eta) = 0, \tag{B3e}$$

and $g_r(0) = 0, g_z'(0) = 0, G_r(D) = 0, G_z(D) = 0$, the equations can be solved in terms of modified Bessel functions. The internal flow admits the general solution

$$g_r(r) = a_1 K_1\left(\epsilon^{1/2}kr\right) + a_2 I_1\left(\epsilon^{1/2}kr\right) + a_3 rK_0\left(\epsilon^{1/2}kr\right) + a_4 rI_0\left(\epsilon^{1/2}kr\right), \tag{B4a}$$

$$g_z(r) = a_1\epsilon^{1/2}K_0\left(\epsilon^{1/2}kr\right) - a_2\epsilon^{1/2}I_0\left(\epsilon^{1/2}kr\right) - \frac{2a_3}{k}K_0\left(\epsilon^{1/2}kr\right) + a_3\epsilon^{1/2}rK_1\left(\epsilon^{1/2}kr\right)$$

$$- \frac{2a_4}{k}I_0\left(\epsilon^{1/2}kr\right) - a_4\epsilon^{1/2}rI_1\left(\epsilon^{1/2}kr\right), \tag{B4b}$$

$$ih(r) = -2\epsilon\left(a_3 K_0\left(\epsilon^{1/2}kr\right) + a_4 I_0\left(\epsilon^{1/2}kr\right)\right). \tag{B4c}$$

The solution set is linearly independent since the Wronskian $W = -4k^2\epsilon/r^2$ is non-zero. Symmetry along $r = 0$ requires $a_1 = a_3 = 0$. Similarly, we obtain the general solution for the extrusive velocities and pressure as

$$G_r(r) = b_1 K_1\left(\epsilon^{1/2}kr\right) + b_2 I_1\left(\epsilon^{1/2}kr\right) + b_3 rK_0\left(\epsilon^{1/2}kr\right) + b_4 rI_0\left(\epsilon^{1/2}kr\right), \tag{B5a}$$

$$G_z(r) = \frac{1}{\epsilon}\left[b_1\epsilon^{1/2}K_0\left(\epsilon^{1/2}kr\right) - b_2\epsilon^{1/2}I_0\left(\epsilon^{1/2}kr\right) - \frac{2b_3}{k}K_0\left(\epsilon^{1/2}kr\right)\right.$$

$$\left. + b_3\epsilon^{1/2}rK_1\left(\epsilon^{1/2}kr\right) - \frac{2b_4}{k}I_0\left(\epsilon^{1/2}kr\right) - b_4\epsilon^{1/2}rI_1\left(\epsilon^{1/2}kr\right)\right], \tag{B5b}$$

$$iH(r) = -2\left(b_3 K_0\left(\epsilon^{1/2}kr\right) + b_4 I_0\left(\epsilon^{1/2}kr\right)\right). \tag{B5c}$$

Applying the interfacial boundary conditions and no-slip, no-penetration outer conditions, a linear system is derived for the coefficients $a_{2,4}, b_{1-4}$

$$
\boldsymbol{A}\begin{pmatrix} a_2 \\ a_4 \\ b_1 \\ b_2 \\ b_3 \\ b_4 \end{pmatrix} = \begin{pmatrix} 0 \\ -\frac{\eta}{2}(1-\epsilon)(1-\lambda) \\ 0 \\ 1 \\ 0 \\ 0 \end{pmatrix}, \tag{B6}
$$

where

$$
\boldsymbol{A} = \begin{pmatrix}
I_1 & I_0\eta & -K_1 & -I_1 & -K_0\eta & -I_0\eta \\
A_{21} & A_{22} & A_{23} & A_{24} & A_{25} & A_{26} \\
A_{31} & A_{32} & A_{33} & A_{34} & A_{35} & A_{36} \\
A_{41} & A_{42} & A_{43} & A_{44} & A_{45}, & A_{46} \\
0 & 0 & K_1(\epsilon^{1/2}Dk) & I_1(\epsilon^{1/2}Dk) & DK_0(\epsilon^{1/2}Dk) & DI_0(\epsilon^{1/2}Dk) \\
0 & 0 & K_0(\epsilon^{1/2}Dk) & -I_0(\epsilon^{1/2}Dk) & A_{65} & A_{66}
\end{pmatrix} \tag{B7}
$$

with $I_0 = I_0(\epsilon^{1/2}\eta k)$, $I_1 = I_1(\epsilon^{1/2}\eta k)$, $K_0 = K_0(\epsilon^{1/2}\eta k)$, $K_1 = K_1(\epsilon^{1/2}\eta k)$ and

$$
\left.\begin{aligned}
A_{21} &= \epsilon^{1/2}I_0, \quad A_{22} = 2\frac{I_0}{k} + \epsilon^{1/2}I_1\eta, \quad A_{23} = \epsilon^{1/2}K_0, \\
A_{24} &= -\epsilon^{1/2}I_0, \quad A_{25} = -2\frac{K_0}{k} + \epsilon^{1/2}K_1\eta, \quad A_{26} = -2\frac{I_0}{k} - \epsilon^{1/2}I_1\eta, \\
A_{31} &= \frac{2}{\eta}\left(-\epsilon I_1 + \epsilon^{3/2}I_0k\eta\right), \quad A_{32} = 2\epsilon^{3/2}I_1k\eta, \quad A_{33} = \frac{2}{\eta}\left(K_1 + \epsilon^{1/2}K_0k\eta\right), \\
A_{34} &= \frac{2}{\eta}\left(I_1 - \epsilon^{1/2}I_0k\eta\right), \quad A_{35} = 2\epsilon^{1/2}K_1k\eta, \quad A_{36} = -2\epsilon^{1/2}I_1k\eta, \\
A_{41} &= -2\epsilon I_1k, \quad A_{42} = -2\epsilon^{1/2}I_1 - 2\epsilon I_0k\eta, \quad A_{43} = 2K_1k, \\
A_{44} &= 2I_1k, \quad A_{45} = -\frac{2}{\epsilon^{1/2}}K_1 + 2K_0k\eta, \quad A_{46} = \frac{2I_1}{\epsilon^{1/2}} + 2I_0k\eta, \\
A_{65} &= \frac{1}{\epsilon^{1/2}k}\left(-2K_0(\epsilon^{1/2}Dk) + \epsilon^{1/2}DkK_1(\epsilon^{1/2}Dk)\right), \\
A_{66} &= \frac{1}{\epsilon^{1/2}k}\left(-2I_0(\epsilon^{1/2}Dk) - \epsilon^{1/2}DkI_1(\epsilon^{1/2}Dk)\right).
\end{aligned}\right\} \tag{B8}
$$

Varying ϵ, D leads to changes in the dispersion curves from the conduit dispersion relation as well as changes in the critical frequency ω_{cr}, critical wavenumber k_{cr} and inflection point k_{inf} (see figure 18).
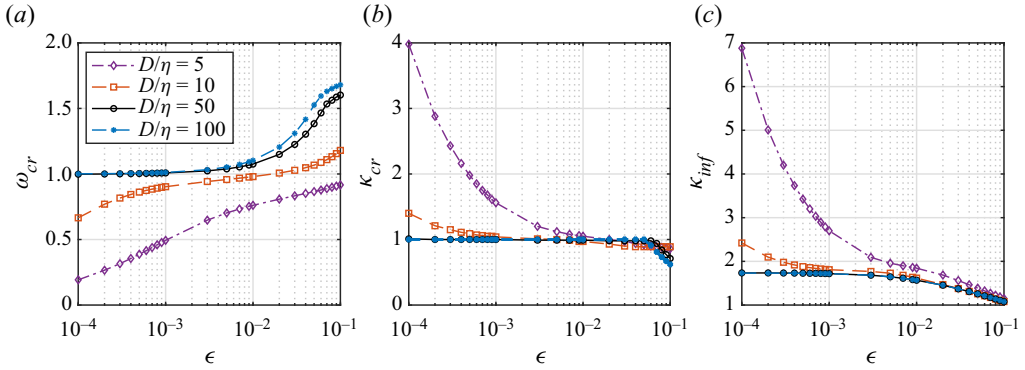
954 A14-29

Figure 18. Investigation of (a) the critical frequency ω_{cr}, (b) the critical wavenumber k_{cr} and (c) the inflection point k_{inf} at selected parameters ϵ, D for recirculating flow (2.11).

Following the asymptotic behaviour $D = \epsilon^{-1/2}d$ and $\lambda = \epsilon(16/d^2) + O(\epsilon^2 \ln(\epsilon))$, where $d = O(1)$, we expand the modified Bessel functions in the linear system (B6) for $\epsilon \to 0$. We seek solutions to the system (B6) with the asymptotic expansions

$$
\boldsymbol{v} = \begin{pmatrix} a_2 \\ a_4 \\ b_1 \\ b_2 \\ b_3 \\ b_4 \end{pmatrix} = \begin{pmatrix} \epsilon^{-3/2}\left(a_{20} + \epsilon \ln(\epsilon)a_{21} + \epsilon a_{22} + \epsilon^2 \ln(\epsilon)a_{23} + \epsilon^2 a_{24} + \dots\right) \\ \epsilon^{-1}\left(a_{40} + \epsilon \ln(\epsilon)a_{41} + \epsilon a_{42} + \epsilon^2 \ln(\epsilon)a_{43} + \epsilon^2 a_{44} + \dots\right) \\ \epsilon^{1/2}\left(b_{10} + \epsilon \ln(\epsilon)b_{11} + \epsilon b_{12} + \epsilon^2 \ln(\epsilon)b_{13} + \epsilon^2 b_{14} + \dots\right) \\ \epsilon^{1/2}\left(b_{20} + \epsilon \ln(\epsilon)b_{21} + \epsilon b_{22} + \epsilon^2 \ln(\epsilon)b_{23} + \epsilon^2 b_{24} + \dots\right) \\ \epsilon\left(b_{30} + \epsilon \ln(\epsilon)b_{31} + \epsilon b_{32} + \epsilon^2 \ln(\epsilon)b_{33} + \epsilon^2 b_{34} + \dots\right) \\ \epsilon\left(b_{40} + \epsilon \ln(\epsilon)b_{41} + \epsilon b_{42} + \epsilon^2 \ln(\epsilon)b_{43} + \epsilon^2 b_{44} + \dots\right) \end{pmatrix}. \quad \text{(B9)}
$$

Collecting (B6) with (B9) at each order and applying the kinematic boundary condition (B3a), we achieve the asymptotic expression (2.17) for the linear dispersion relation with

$$
\begin{aligned}
\omega_2(k) = {} & 4k\left(-1 + \ln\left(\frac{d}{2\sqrt{2}}\right)\right) - \frac{\sqrt{2}k(1 + 2k^2)}{1 + k^2}b_{20} - 2\sqrt{2}b_{40} \\
& + \frac{2k}{3d^2(1 + k^2)^2}\Big[d^2\Big(6\Gamma\left(k^4 - 2k^2 - 1\right) \\
& + k^4(\ln(8) - 19) - 6k^2(4 + \ln(2)) - 6 - \ln(8)\Big) \\
& + 6d^2\left(k^4 - 2k^2 - 1\right)\ln(k) - 48\left(k^2 + 1\right)\Big],
\end{aligned} \quad \text{(B10)}
$$

where Γ is the Euler–Mascheroni constant ($0.5772\ldots$) and the coefficients are

$$\left.\begin{aligned}
b_{10} &= -\frac{4\sqrt{2}k^2}{1+k^2}, \\[4pt]
b_{20} &= \frac{\begin{aligned}I_0(dk)\left(K_1(dk)\left(d^2kb_{30}+2b_{10}\right)+dkb_{10}K_0(dk)\right)+dkI_1(dk)(b_{10}K_1(dk)\\+db_{30}K_0(dk))\end{aligned}}{dkI_0(dk)^2-2I_1(dk)I_0(dk)-dkI_1(dk)^2}, \\[4pt]
b_{30} &= -\frac{\sqrt{2}k(1+3k^2)}{1+k^2}, \\[4pt]
b_{40} &= -\frac{\begin{aligned}kI_0(dk)(b_{10}K_1(dk)+db_{30}K_0(dk))+I_1(dk)(K_0(dk)(kb_{10}-2b_{30})\\+dkb_{30}K_1(dk))\end{aligned}}{dkI_0(dk)^2-2I_1(dk)I_0(dk)-dkI_1(dk)^2}.
\end{aligned}\right\} \tag{B11}$$

REFERENCES

ANDERSON, D.V., MAIDEN, M.D. & HOEFER, M.A. 2019 Controlling dispersive hydrodynamic wavebreaking in a viscous fluid conduit. *Phys. Rev. Fluids* **4** (7), 074804.

BATCHELOR, G.K. & GILL, A.E. 1962 Analysis of the stability of axisymmetric jets. *J. Fluid Mech.* **14** (4), 529–551.

BENJAMIN, T.B., BONA, J.L. & MAHONY, J.J. 1972 Model equations for long waves in nonlinear dispersive systems. *Phil. Trans. R. Soc. Lond.* A **272** (1220), 47–78.

BÜHLER, O. 2014 *Waves and Mean Flows*. Cambridge University Press.

CAMASSA, R. & OGROSKY, H.R. 2015 On viscous film flows coating the interior of a tube: thin-film and long-wave models. *J. Fluid Mech.* **772**, 569–599.

CHABCHOUB, A., HOFFMANN, N.P. & AKHMEDIEV, N. 2011 Rogue wave observation in a water wave tank. *Phys. Rev. Lett.* **106** (20), 204502.

CHWANG, A.T. 1983*a* Nonlinear hydrodynamic pressure on an accelerating plate. *Phys. Fluids* **26** (2), 383–387.

CHWANG, A.T. 1983*b* A porous-wavemaker theory. *J. Fluid Mech.* **132**, 395–406.

EL, G.A. & HOEFER, M.A. 2016 Dispersive shock waves and modulation theory. *Physica* D **333**, 11–65.

GASTER, M. 1962 A note on the relation between temporally-increasing and spatially-increasing disturbances in hydrodynamic stability. *J. Fluid Mech.* **14** (2), 222–224.

GORING, D. & RAICHLEN, F. 1980 The generation of long waves in the laboratory. In *Coastal Engineering 1980*, vol. 1, pp. 763–783. ASCE.

HARRIS, S.E. & CLARKSON, P.A. 2006 Painlevé analysis and similarity reductions for the magma equation. *Symmetry Integr. Geom.* **2**, 068.

HELFRICH, K.R. & WHITEHEAD, J.A. 1990 Solitary waves on conduits of buoyant fluid in a more viscous fluid. *Geophys. Astrophys. Fluid Dyn.* **51** (1–4), 35–52.

HICKOX, C.E. 1971 Instability due to viscosity and density stratification in axisymmetric pipe flow. *Phys. Fluids* **14** (2), 251–262.

JOHNSON, M.A. & PERKINS, W.R. 2020 Modulational instability of viscous fluid conduit periodic waves. *SIAM J. Math. Anal.* **52** (1), 277–305.

JOSEPH, D.D., BAI, R., CHEN, K.P. & RENARDY, Y.Y. 1997 Core-annular flows. *Annu. Rev. Fluid Mech.* **29** (1), 65–90.

KORTEWEG, D.J. & DE VRIES, G. 1895 XLI. On the change of form of long waves advancing in a rectangular canal, and on a new type of long stationary waves. *Lond. Edinb. Dublin Philos. Mag. J. Sci.* **39** (240), 422–443.

KUMAGAI, I. & KURITA, K. 1998 Interaction of periodic wave trains in magma conduits. *Phys. Earth Planet. Inter.* **107** (1–3), 131–141.

KURAMOTO, Y. 1978 Diffusion-induced chaos in reaction systems. *Prog. Theor. Phys. Suppl.* **64**, 346–367.

LOWMAN, N.K. & HOEFER, M.A. 2013 Dispersive hydrodynamics in viscous fluid conduits. *Phys. Rev.* E **88** (2), 023016.

LOWMAN, N.K., HOEFER, M.A. & EL, G.A. 2014 Interactions of large amplitude solitary waves in viscous fluid conduits. *J. Fluid Mech.* **750**, 372–384.

MAIDEN, M.D., ANDERSON, D.V., FRANCO, N.A., EL, G.A. & HOEFER, M.A. 2018 Solitonic dispersive hydrodynamics: theory and observation. *Phys. Rev. Lett.* **120** (14), 144101.

MAIDEN, M.D., FRANCO, N.A., WEBB, E.G., EL, G.A. & HOEFER, M.A. 2020 Solitary wave fission of a large disturbance in a viscous fluid conduit. *J. Fluid Mech.* **883**, A10.

MAIDEN, M.D. & HOEFER, M.A. 2016 Modulations of viscous fluid conduit periodic waves. *Proc. R. Soc. Lond.* A **472** (2196), 20160533.

MAIDEN, M.D., LOWMAN, N.K., ANDERSON, D.V., SCHUBERT, M.E. & HOEFER, M.A. 2016 Observation of dispersive shock waves, solitons, and their interactions in viscous fluid conduits. *Phys. Rev. Lett.* **116** (17), 174501.

D'OLCE, M., MARTIN, J., RAKOTOMALALA, N., SALIN, D. & TALON, L. 2009 Convective/absolute instability in miscible core-annular flow. Part 1:eExperiments. *J. Fluid Mech.* **618**, 305–322.

OLSON, P. & CHRISTENSEN, U. 1986 Solitary wave propagation in a fluid conduit within a viscous matrix. *J. Geophys. Res.* **91** (B6), 6367–6374.

REDOR, I., BARTHÉLEMY, E., MICHALLET, H., ONORATO, M. & MORDANT, N. 2019 Experimental evidence of a hydrodynamic soliton gas. *Phys. Rev. Lett.* **122** (21), 214502.

SCOTT, D.R., STEVENSON, D.J. & WHITEHEAD, J.A. 1986 Observations of solitary waves in a viscously deformable pipe. *Nature* **319** (6056), 759–761.

SELVAM, B., TALON, L., LESSHAFFT, L. & MEIBURG, E. 2009 Convective/absolute instability in miscible core-annular flow. Part 2. Numerical simulations and nonlinear global modes. *J. Fluid Mech.* **618**, 323–348.

SIMPSON, G. & WEINSTEIN, M.I. 2008 Asymptotic stability of ascending solitary magma waves. *SIAM J. Math. Anal.* **40** (4), 1337–1391.

SIVASHINSKY, G.I. 1977 Nonlinear analysis of hydrodynamic instability in laminar flames—I. Derivation of basic equations. *Acta Astronaut.* **4**, 1177–1206.

SOMMERFELD, A. 1912 Die greensche funktion der schwingungsgleichung. *J.-Ber. Deutsch Math.-Verein* **21**, 309–353.

SOMMERFELD, A. 1949 *Partial Differential Equations in Physics*. Academic.

STUBBLEFIELD, A.G., SPIEGELMAN, M. & CREYTS, T.T. 2020 Solitary waves in power-law deformable conduits with laminar or turbulent fluid flow. *J. Fluid Mech.* **886**, A10.

TIKAN, A., *et al.* 2022 Prediction and manipulation of hydrodynamic rogue waves via nonlinear spectral engineering. *Phys. Rev. Fluids* **7** (5), 054401.

TRILLO, S., DENG, G., BIONDINI, G., KLEIN, M., CLAUSS, G.F., CHABCHOUB, A. & ONORATO, M. 2016 Experimental observation and theoretical description of multisoliton fission in shallow water. *Phys. Rev. Lett.* **117** (14), 144102.

WHITEHEAD, J.A. & HELFRICH, K.R. 1986 The Korteweg-deVries equation from laboratory conduit and magma migration equations. *Geophys. Res. Lett.* **13** (6), 545546.

WHITEHEAD, J.A. & HELFRICH, K.R. 1990 Magma waves and diapiric dynamics. In *Magma Transport and Storage* (ed. M.P. Ryan), pp. 53–76. John Wiley & Sons.

WHITHAM, G.B. 1974 *Linear and Nonlinear Waves*. John Wiley & Sons Inc.

YIH, C.-S. 1963 Stability of liquid flow down an inclined plane. *Phys. Fluids* **6** (3), 321–334.

YIH, C.-S. 1967 Instability due to viscosity stratification. *J. Fluid Mech.* **27** (2), 337–352.